The Thesis Committee for Scott Sumner Haltom
Certifies that this is the approved version of the following thesis:

On the Ductile Failure of Thin-Walled Aluminum Alloy Tubes Under Combined Shear and Tension

APPROVED BY
SUPERVISING COMMITTEE:

Supervisor:

Stelios Kyriakides, Supervisor

Krishnaswamy Ravi-Chandar

On the Ductile Failure of Thin-Walled Aluminum Alloy Tubes Under Combined Shear and Tension

by

Scott Sumner Haltom, BS

Thesis

Presented to the Faculty of the Graduate School of

The University of Texas at Austin

in Partial Fulfillment

of the Requirements

for the Degree of

Master of Science in Engineering

The University of Texas at Austin

December 2012

Acknowledgements

I would like to express my appreciation to my adviser, Professor Stelios Kyriakides for his guidance and teaching over the past two years. I have gained a tremendous amount of knowledge regarding engineering mechanics theory and experimental procedure. I would also like to thank Professor Krishnaswamy Ravi-Chandar for his assistance. Dr Ravi-Chandar particularly helped me with the microscopic investigations seen in this thesis and also served as my second reader. The financial support from the Office of Naval Research through the MURI project N00014-06-1-0505-A00001 as well is much appreciated.

Additionally, I could not have achieved this without the tremendous help given by the machinists Travis Crooks, Ricardo Palacios, and Joe Pokluda as well as the electronics expertise of Pablo Cortez. I truly appreciate their patience and understanding, not to mention their excellent work. I would also like to extend a special thanks to my friends and fellow graduate students, especially Theofilos Giagmouris for helping me get started with the project and Andrew Barnes for going out of his way to help me with the metallographic analysis.

Finally, I would especially like to thank my friends and family for their patience and support. Without y'all, I would not have been able to accomplish many of the things in my life.

Abstract

On the Ductile Failure of Thin-Walled Aluminum Alloy Tubes Under Combined Shear and Tension

Scott Sumner Haltom, MSE

The University of Texas at Austin, 2012

Supervisor: Stelios Kyriakides

The aim of this thesis is to establish the extent to which materials can be deformed under shear-dominant loadings. Custom Al-6061-T6 tubular specimens are loaded under radial and corner paths of tension and shear to failure. During the experiments, the deformation is monitored in a test section designed to have nearly uniform stress and deformation at large strains while providing minimum constraint to the development of localization that precedes failure. The recorded shear stress-rotation and axial stress-displacement responses exhibit maxima beyond which deformation localizes in a narrow band that is of the order of the 1 mm wall thickness of the test section. For the mainly shear dominated stress paths followed, deformation remained nearly planar allowing for the establishment of both the true stresses and the local deformation strictly from measurements. Results from thirteen radial path experiments as well as from four corner path experiments show the strain at failure to monotonically increase as the mean stress decreases, a result that is in contrast with previously reported results for Al alloys. Also, the measured failure strains are significantly larger than previously reported values. Analysis of corner stress paths investigates the path dependence of localization and failure. Results show little path dependence on the failure strains, but some path dependence on stress maxima and failure stresses. Furthermore,

statistical grain-level strain estimates from five of the stress paths revealed a significant variation in strain across the macroscopically observed localization zone. In the neighborhood of the crack tip strains with 25-100% higher levels than the macroscopic values were recorded. This indicates that localization also occurs at a smaller scale than hitherto understood. The difference between the macro strain at failure and the average grain level values increased as the axial/shear stress ratio increased.

Table of Contents

Chapter 1: Introduction

Despite more than 50 years of progress, establishing the onset of failure in ductile metals remains a challenge, hampering design in important industrial processes. Although the issue was first raised by McClintock [1971], Wierzbicki and coworkers (e.g., Bao and Wierzbicki [2004], Bai and Wierzbicki [2008, 2010]) must be credited for bringing to fore the idea that failure may not be simply dependent on stress triaxiality as purported by the commonly used Johnson-Cook failure criterion [1985] (influenced by the pioneering work of McClintock [1968], Rice and Tracy [1969] and others). Particularly problematic are shear-dominated stress states with low triaxiality. This gave impetus to a number of efforts, a few experimental but most analytical/numerical, which, in addition to mean stress, consider the effect of J_3, the third invariant of the deviatoric stress tensor (or through the non-dimensional variable θ defined in Eq. (3e)).

Experiments under combined axial and shear loads where the true stresses and deformations are followed up to the onset of failure are difficult to perform and should have the following characteristics: (a) The test section must have a finite domain of uniform stress and must be free of stress concentrations. (b) In addition, the test section must be wide enough for the localizations to develop naturally, free of geometric constraints. (c) The induced relatively large deformation must be accurately measured during the initial uniform regime as well as subsequently when localization sets in, often in a relatively narrow zone. Moreover, because the manufacture and processing of bulk materials usually leads to texturing and anisotropy that is unique to each process, the specimens must come from the same stock (we are particularly referring here to differences between sheet, tube and solid rod stock). Some of the most quoted experiments (e.g., Bao and Wierzbicki [2004], Barsoum and Faleskog [2007], Beese *et al.* [2010]) do not satisfy one or more of these requirements.

Modeling of experiments or the use of FE models to extract the stress and deformations at failure, must overcome equally high challenges. First, the material stress-strain response at large strains must be established accurately; this because both the

material response under multiaxial loadings and, even more importantly, localization are sensitive to the plastic modulus at large strains. Since such extractions usually come from the 3-D deformation and stress inside a diffuse neck or other type of localization formed in tensile tests on rod or sheet specimens, the challenge becomes more acute (see recent works by Dunand and Mohr [2010], Tardif and Kyriakides [2012]). Second, plastic anisotropy plays an important role in the behavior of the material in biaxial tests and influences the extracted stress-strain response. It must, therefore, be characterized and incorporated in the modeling. Third, it has now been well established that in several families of alloys, plastic deformation and anisotropy are not adequately captured by J_2 plasticity or Hill-1948 anisotropy. This has been demonstrated most prominently in the case of Al alloys where its influence on the prediction of the material response under multiaxial loadings (e.g., Korkolis and Kyriakides [2008a, 2008b], Korkolis *et al.* [2010]) and more prominently on localization (Giagmouris *et al.,* 2010) was shown to be significant.

Mohr and co-workers have taken a much more careful alternate approach to the testing of sheet stock to failure under combined shear and axial loads. Although their specimen design has evolved (Mohr and Henn [2007], Mohr and Oswald [2008], Dunand and Mohr [2011]), they employ a butterfly shaped specimen designed to have the desired shear-axial stress in its narrow center. The deformation is monitored with DIC while the evolving state of stress is determined from a FE model of the test. This test set up is clearly dependable for constitutive modeling; however, they point out that getting failure to consistently occur in the central part of the test section is difficult for shear-dominated loadings. Furthermore, it is not clear that the design does not inhibit the development of localization.

The objective of this work is to develop a test suited for shear/axial loading of a thin-walled solid to failure that satisfies the requirements outlined above. Additionally, the stresses and deformations are to be determined strictly from the experiment. The most direct way to achieve uniform shear is by twisting a thin walled tube. Thus, combined axial-torsional loadings have long been one of the most widely used tests for constitutive

modeling of solids in the plastic regime. The challenge here is that we require that the specimen be loaded heavily into the plastic regime, where the ensuing localized deformation develops freely, and the onset of failure can be captured. This thesis presents a custom tubular specimen design that achieves these requirements and presents results of failure strains for a series of combined shear-tension loading histories.

Chapter 2: Experimental

Chapter 2: provides a detailed description of the experimental set-up, specimen design, as well as the formulas used to calculate the stresses and deformations. The experimental set-up was designed to effectively measure the stresses and deformations in the gage section of a specially designed thin-walled aluminum tube specimen under combined axial and torsional loading. Several unique methods were developed to ensure accurate stress and deformation measurements could be taken directly from the experimental data.

2.1 Set-up and Procedures

The experiments are conducted on commercially available 2-inch diameter Al-6061-T6 seamless drawn tubes with a nominal wall thickness of 0.125 in (3.2 mm). Nine-inch (229 mm) test specimens are cut from 12 ft (3.65 m) long mother tubes. A test section of approximately 0.040 in (1.02 mm) thick and 0.6 in (15.3 mm) wide is machined a mid-length as shown in Figure 2.1. It has a 0.400 in (10.2 mm) wide uniform thickness section that ends in 0.125 in (3.2 mm) radii on either end. The particular geometry was designed to maintain nearly uniform planar stress levels in the test section and avoid torsional buckling. The machining is performed using the internal diameter as reference in order to ensure minimum wall eccentricity of the test section (typically eccentricity ~1%).

The specimen is mounted onto a MTS servohydraulic axial/torsional biaxial testing machine with capacities of 50 kip/22 in-kip (220 kN/2.5 m-kN). The biaxial loading applied leads to localization of deformation followed by rupture. Accurately recording the evolution of localized deformation up to the onset of failure requires a stiff testing system, very good alignment of the specimen with the testing machine, and

special loading procedures. The first two requirements were met by developing the custom gripping fixtures shown in Figure 2.2. They consist of two high-precision ETP-TECHNO axisymmetric clamps[1] shown in Figure 2.2 and Figure 2.3. They are 80 mm (3.15 in) deep with a 50.0 mm (1.9685 in) ID and 65.0 mm (2.559 in) OD. The thicker part of the 9-inch specimen is inserted into the clamps, which engage heavy steel housings on the outside. Integral to the clamps are thin inner and outer shells separated from the main body by an oil-based fluid. By employing a small screw-driven piston, the cavities expand, clamping both the specimen and the housing. Tight fitting aluminum plugs are inserted inside the gripped sections of the test specimen to reduce the compliance of the tube and prevent slipping. Effective gripping also requires that the diameters of the housing ID, the OD of the specimen and that of the solid plugs be machined to a tolerance of the order of 0.001 in (25 μm). The upper and lower grips were initially aligned using a precision solid rod.

During the experiment, the axial force and torque as well as the corresponding axial and rotational displacements are monitored respectively by a biaxial load cell and displacement transducers integral to the testing machine. The load cell signals, together with those of the rotation and axial displacement transducers, are monitored in real time using a computer based data acquisition system where they are also stored for later processing. More local measurements of deformation within the test section will be described separately. The majority of tests reported here involve radial loading in the nominal shear-axial stress ($\mathcal{T}$ - Σ) space so that

$$\Sigma = \alpha \mathcal{T} \qquad \alpha = \text{const.} > 0. \tag{1}$$

This is achieved as follows: torsion is run under rotation control and axial load under load control. The two loads are coupled by using the torque as command signal for the axial

[1] Several experiments were performed using standard *Ringfeder* style grips. The *Ringfeder* grips, however, were found to be insufficient for the test. They could not provide the necessary concentricity and repeatability that is demanded by the test; although small, additional stresses were applied to the specimens by the misalignment and several experiments failed unexpectedly and the tests were not repeatable. The ETP TECHNO clamps, on the other hand, provided the tight tolerance required and repeatabilitable experiments.

load loop resulting in a force appropriately proportional to the torque (e.g., see Korkolis and Kyriakides [2008a] for corresponding axial load-internal pressure set up).

Four additional experiments were executed following corner paths as follows. The experiments corresponded to the radial paths α = 1.0 and 1.5. In the first corner path the tube was torqued at zero axial stress until the induced shear stress reached the level at which the tube failed in the corresponding radial path. At this point, the shear stress was held constant, under torque control, and the tube was loaded axially under displacement control. This loading was continued until the specimen localized and ultimately developed a failure crack. This loading corresponds with the path OBC in Figure 2.4. In the alternate corner path, the specimen was preloaded axially under zero torque until the failure stress for the corresponding radial path was reached. Subsequently, the axial stress was held constant under load control while the tube was rotated under rotation control until failure. This loading corresponds with the path ODE in Figure 2.4.

In the experiments performed, of main interest is the deformation in the 0.400 in (10 mm) wide part of the test section with constant thickness. It initially undergoes uniform shearing and stretching but later yields to rather large localized deformations that eventually result in local rupture. Localization covers a narrow band that is of the order of the 0.040 in (1.0 mm) wall thickness, making measurements with usual techniques difficult. Thus, we opted to measure the deformation by monitoring the distortion of a fine grid placed in the test section by electro-etching. The grid, shown in Figure 2.1b, is square with 0.03125 in (0.794 mm) sides. It is photographed at regular intervals (typically 5 s) using a high-resolution digital camera (4288 × 2848 pixels) operated by a laptop equipped with a timer. The timer and the data acquisition system have a common time base, which allows synchronization of recorded loads and displacements with the deformed grid images. The images are subsequently processed to yield the strains as described in Section 3.1.

The elongation of the test section is also monitored using an EIR Model LE-05 non-contact laser extensometer. The laser extensometer scans at a rate of 100 scans/sec and measures the distance between two strips of retro-reflective tape. The laser is

mounted on a tripod such that the receiver is 12 in away from the target. The laser outputs the measurements in the standard 10V full scale. With the chosen settings, the laser has a full scale reading of 0.1 in (2.5 mm) and a resolution of 0.0001 in (25 μm). Because the test section undergoes rotation, the targets consist of two retro-reflective strips, approximately 1.5 in (38 mm) apart, mounted on two rings that are clamped to the thicker parts of the tube on either side of the test section (see Figure 2.3). The stationary laser monitors the distance between the rotating strips.

2.2 STRESSES AND DEFORMATIONS

Let σ_{ij} represent the Cauchy stress components, s_{ij} the deviatoric components and σ_i and s_i the corresponding principal values. The test set up is such that in the test section the through-thickness stress is essentially zero, and its radius remains unchanged. Thus the stresses are:

$$\sigma_{11} = \sigma, \quad \sigma_{22} = \sigma/2, \quad \sigma_{12} = \tau \tag{2}$$

and other components are zero. The principal stresses are

$$\sigma_{1,2} = \frac{3}{4}\sigma \pm \sqrt{\frac{\sigma^2}{16} + \tau^2} \tag{3a}$$

The key stress measures take the following form:

Mean stress: $$\sigma_m = tr(\boldsymbol{\sigma})/3 = \sigma/2 \tag{3b}$$

Equivalent stress: $$\sigma_e = \sqrt{\frac{3}{2}(\boldsymbol{s}:\boldsymbol{s})} = \sqrt{\frac{3}{4}(\sigma^2 + 4\tau^2)} \tag{3c}$$

J_3: $$J_3 = s_1 s_2 s_3 = (\sigma_1 - \sigma_m)(\sigma_2 - \sigma_m)(\sigma_3 - \sigma_m) = \frac{\sigma\tau^2}{2} \tag{3d}$$

Haigh-Westergaard variable θ: $$\cos 3\theta = \left(\frac{27}{2}\frac{J_3}{\sigma_e^3}\right) = \frac{6\sqrt{3}\sigma\tau^2}{(\sigma^2 + 4\tau^2)^{3/2}} \tag{3e}$$

and $\bar{\theta} = 1 - \frac{6\theta}{\pi}$ (from Wierzbicki and co-workers).

Nahshon-Hutchinson (2008) parameter ω: $\omega = 1 - \cos^2 3\theta$ (3f)

The test leads to rather large deformations in the test section that are established from the deformed grid. Figure 2.5 shows schematically the grid undeformed (a), sheared and stretched uniformly (b), and the configuration it acquires once localization sets in (c). The deformation gradient tensor **F** is established from the deformed grid as follows. Let the initially square grid deform in the $(\boldsymbol{e}_1, \boldsymbol{e}_2)$ plane as shown in Figure 2.6. The deformation is then given by

$$\mathbf{y} = \mathbf{F}\mathbf{x} = \begin{bmatrix} 1 & k & 0 \\ 0 & a & 0 \\ 0 & 0 & b \end{bmatrix} \begin{Bmatrix} x_1 \\ x_2 \\ x_3 \end{Bmatrix} \tag{4}$$

The constants k and a are established from the deformed grid using the NIH software *ImageJ*, and b is chosen to satisfy incompressibility. While the deformation is uniform (Figure 2.5b), measurements over the full gage length are preferred. Once localization sets in (Figure 2.5c), the deformation variables are based on local measurements involving only a few deformed blocks. In the latter case, the measurements are taken from the neighborhood where localization is more prominent leading eventually to failure. For both sets of measurements, k and a are average values over several grid measurements. The principal stretches and logarithmic strains, λ_i and e_i $i = 1,3$ respectively, are evaluated from **F** as described below.

The Lagrangian strain tensor is evaluated from the deformation gradient in (4) as follows

$$= \frac{1}{2}[\mathbf{F}^T\mathbf{F} - 1] = \frac{1}{2}\begin{bmatrix} 0 & k & 0 \\ k & k^2 + a^2 - 1 & 0 \\ 0 & 0 & b^2 - 1 \end{bmatrix} \tag{4a}$$

The principal values of the strain tensor, δ_i, are evaluated from:

$$\det|\boldsymbol{\varphi}-\delta\mathbf{I}| = \begin{vmatrix} -\delta & k/2 & 0 \\ k/2 & (k^2+a^2-1)/2-\delta & 0 \\ 0 & 0 & (b^2-1)/2-\delta \end{vmatrix} \tag{4b}$$

They take values of

$$\delta_{1,2} = \left(\frac{k^2+a^2-1}{4}\right) \pm \frac{1}{2}\sqrt{\frac{1}{4}(k^2+a^2-1)^2+k^2} \quad \text{and} \quad \delta_3 = \frac{b^2-1}{2} \tag{4c}$$

The principal stretches, λ_i are then given by

$$\mathbf{C}^{pr} = \begin{bmatrix} \lambda_1^2 & 0 & 0 \\ 0 & \lambda_2^2 & 0 \\ 0 & 0 & \lambda_3^2 \end{bmatrix} = \begin{bmatrix} 2\delta_1+1 & 0 & 0 \\ 0 & 2\delta_2+1 & 0 \\ 0 & 0 & 2\delta_3+1 \end{bmatrix} \tag{4d}$$

Elastic deformations are small by comparison and are neglected. If in addition incompressibility of plastic deformations is assumed then

$$\lambda_3 = (\lambda_1\lambda_2)^{-1}$$

and the logarithmic principal strains become:

$$e_1 = \ln\lambda_1, \; e_2 = \ln\lambda_2 \text{ and } e_3 = -(e_1+e_2) \tag{4e}$$

The stress variables σ and τ are evaluated from the measured torque (T) and axial force (F) as follows:

$$\sigma = \frac{F}{2\pi R_o t_o}\frac{1}{\lambda_3} \quad \text{and} \quad \tau = \frac{T}{2\pi R_o^2 t_o}\frac{1}{\lambda_3} \tag{5}$$

where R_o and t_o are the initial radius and wall thickness of the test section.

Chapter 3: Tension-Torsion Results

The experimental set-up and methods described in Chapter 2 were utilized to test seventeen Al 6061-T6 2-inch diameter drawn tubular specimens under tension and torsion until each specimen failed. Of the seventeen experiments, thirteen of them followed a radial or proportional stress path with α values ranging from 0.125 to 2.5, while four experiments followed corner stress paths. Of specific interest for the experiments were the strains at failure for each of the specimens; therefore, special attention was focused on monitoring the deformation in the part of the test section where failure was expected described below. Chapter 3: will feature two example radial path experiments before giving an overview of all radial results in section 3.1.3. Additionally, section 3.2 will give a summary of the four corner path experiments and their results.

3.1 Summary of Results from Radial $\mathcal{T}-\Sigma$ Paths

3.1.1 A Typical Shear Stress Dominant Experiment: $\alpha = 0.5$

Experiment 51 with a stress ratio $\alpha = 0.5$ will be used to describe the events from a typical experiment. The test section diameter (D), wall thickness (t), wall eccentricity (Ξ_o) and other parameters of the experiment are listed in Tables

Table 1. In preliminary experiments it was observed that failure usually initiated on the slightly thinner side of the test section and consequently the digital camera recorded the deforming grid in this neighborhood. The test was run at a rotation rate of 1.25×10^{-5} rad/s, resulting in a shear strain rate of $\dot{\gamma} \approx 2 \times 10^{-4} \mathrm{s}^{-1}$ (while deformation in the gage section was uniform). Figure 3.1a shows the prescribed stress path in the axial-shear stress ($\Sigma - \mathcal{T}$) plane (nominal stress values). The resultant shear stress-rotation ($\mathcal{T}-\phi$) and axial stress-elongation ($\Sigma - \delta$) responses are respectively shown in Figure 3.2a and Figure 3.2b (L_g is the nominal length of the test section taken to be 0.60 in–15.2

mm). The shear response traces the expected trajectory comprised of a linear elastic section followed by some hardening. A load maximum develops at a rotation of about 10^o, indicated on the response by a caret (^). Because of the rotation controlled loading, the subsequent descending part of the response is tracked. The stress initially drops gradually, but decreases more precipitously at higher values of ϕ. The corresponding axial stress-elongation response follows a similar trajectory with the stress maximum occurring at just over $0.03\,\delta/L_g$. Again, rather extended post limit load deformation was recorded. Needless to point out that both ϕ and δ are "machine" deformation measures and consequently are not accurate representations of the deformation in the test section. As mentioned earlier, this will be extracted from the recorded images of the deforming grid.

Eleven images of the grid, out of the 463, recorded are shown in Figure 3.3. The images are expanded views of an area covering approximately 24×7 blocks of the initially 0.03125 in (0.794 mm) square grid (shown undeformed in image ⓪). The rotation and elongation that they correspond to are marked on the responses with solid bullets in Figure 3.2a and Figure 3.2b respectively. Thus, in image ① the test section is already plastically deformed and the grid is seen to have rotated and stretched. In images ②-④ the rotation and stretching progressively grow with the gridlines remaining straight indicating that, as expected, the test section is deforming uniformly. In image ⑤, just beyond the torque and load maxima, the rotated gridlines develop some curvature, a sign that localization at mid-height has commenced. This curvature grows in image ⑥ while in ⑦ and ⑧ the rotated gridlines have developed a narrow zone of inflection that implies shear localization. In images ⑨ and ⑩ the localizing zone becomes more pronounced as the deformation grows precipitously inside it. The localization covers a circumferential band with a width that is of the order of the wall thickness. Immediately after image ⑩, the torque and axial force experienced a sudden partial drop indicated by dashed lines in Figure 3.2. Rotation was terminated and failure in the form of a narrow crack was observed to have developed along the circumferential gridline in the middle of the

localization zone. The crack, which is along the darkest circumferential grid line in the last image (×) in Figure 3.3, had an angular span of about 99°, with the remainder of the localized circumferential band left intact. This partial failure is the result of the "stiff" design of the test setup that limits the amount of energy that becomes available on unloading.

At this stage, the specimen was unloaded and the failure zone was examined more closely. Figure 3.4 shows a photograph of the crack, including its tip. The crack is more obvious on the LHS where discontinuity in the bent gridlines is also observed. It runs along one of the circumferential gridlines and terminates just before the last gridline on the RHS. In this test, thin vertical lines were drawn in the test section adjacent to the edges of the grid. The deformed lines provide another measure of the width of the localization zone. It is estimated to be 0.027 in (0.69 mm) tall. As mentioned, the grid was formed by electro-etching, resulting in small depressions about 0.005 in (125 μm) wide and about 0.0005 in (12.5 μm) deep, such as the one shown in the micrograph in Figure 3.5. Localization, which typically occurred at mid-width of the test section, is imperfection sensitive. Consequently, the gridlines, despite their small size, provided enough of a stress riser to initiate localization and eventually failure. It's interesting to point out that the next level of test section characteristic imperfections are turning marks with an estimated roughness of $R_a \sim 0.4$ μm, in other words, significantly smaller than the gridlines.

The deformation gradient tensor **F** in Eq. (4) was subsequently established from selected images of the deformed grid and the principal stretches and logarithmic strains were evaluated along the stress path. These deformation measures enabled the calculation of the true stresses τ and σ. The calculated values at selected points are marked in Figure 3.1a with solid bullets. They are seen to remain on the same proportional trajectory, but values that are higher than the engineering stress maxima (■) are reported.

For completeness we define the axial nominal strain (ε) and "shear" strain (γ) as

$$\varepsilon = a - 1 \text{ and } \gamma = \tan^{-1}\left(\frac{k}{a}\right) \tag{6}$$

These measures will be used mainly for presentation purposes while a more quantitative measure of the deformation will be reported through the principal stretches. Figure 3.1b shows a plot of γ vs. ε for Exp. 51 extracted from the images. The trajectory is nearly linear. It is important to note that small fluctuations arise from two sources. At small strain values, the deformation measured is limited by the pixel resolution of the image. At high values, when deformation is localized, the accuracy of the measurements is limited by the size of the grid. We reiterate that the emphasis of the present study was establishing the deformation in the neighborhood and at failure, in other words at relatively large strains. The reported γ and ε values at small strains are not accurate enough for calibration of constitutive models. Corrected small strain $\mathcal{T}$-γ and $\sigma - \varepsilon$ responses suitable for constitutive modeling appear in the Appendix.

Marked on the trajectory with the symbol ■ are the values corresponding to the load maxima. They correspond to values of $(\gamma, \varepsilon)_L$ = (0.365, 0.0342) (Tables

Table 1). By contrast, the last point, marked with the symbol "×", came from the image taken at the termination of loading from the neighborhood of the tip of the crack, in this case on the RHS of the image in Figure 3.4. These measurements are designated as the "failure" values and are $(\gamma, \varepsilon)_f$ = (1.10, 0.119) (Table 2). The magnitudes of these values are strikingly large and together with all other results point to the fact that most deformation takes place beyond the load maxima in the localizing zone. The equivalent plastic strain at failure is evaluated from the principal stretches and is given by

$$e^p_{ef} = \left[\frac{2}{3}\left(e_1^2 + e_2^2 + e_3^2\right)\right]_f^{1/2} \tag{7}$$

where e_i are the principal logarithmic strains at failure. In this case, e^p_{ef} = 0.97!

3.1.2 A Typical Axial Stress Dominant Experiment: $\alpha = 1.5$

This section focuses on Experiment 36 as an example of the common behavior observed during a more axially dominant radial stress path; in this case $\alpha = 1.5$. The test section diameter (D), wall thickness (t), wall eccentricity (Ξ_o) and other parameters of the experiment are listed in Tables

Table 1. This test was also run at a rotation rate of 1.25×10^{-5} rad/s, resulting in a shear strain rate of $\dot{\gamma} \approx 2 \times 10^{-4} \mathrm{s}^{-1}$. Figure 3.6a shows the prescribed nominal stress path in the $\Sigma - \mathcal{T}$ plane. The resultant $\mathcal{T} - \phi$ and $\Sigma - \delta$ responses are respectively shown in Figure 3.7a and Figure 3.7b. A shear stress maximum develops at a rotation of about 5.5^{o}, indicated on the response by a caret (^). The corresponding axial stress-elongation response follows a similar trajectory with the stress maximum occurring slightly under $0.05\,\delta / L_g$. Here too, large deformations were observed beyond the limit load.

Twelve images of the grid, out of the 284 recorded, are shown in Figure 3.8. The images are expanded views of an area covering approximately 24×8 blocks of the initially 0.03125 in (0.794 mm) square grid, Image ⓪ was captured after the specimen had exceeded the elastic limit and had already experienced moderate plastic deformation. The rotation and elongation that each image corresponds to are marked on the responses with solid bullets in Figure 3.7a and Figure 3.7b as in the previous case. In images ①-⑥ the rotation and stretching of the grid is reasonably uniform with the gridlines remaining linear, indicating that the test section is deforming uniformly as expected. Beginning with image ⑦, the grid lines develop some localized deformation at mid-height. The onset of bending in the grid lines syncs up quite well with the load maximum, indicated by the caret. Image ⑧ shows only a slight increase in the localized deformation. The center gridlines begin to rapidly bend, however, once the load begins to drop more significantly, as seen in image ⑨ and to an even greater extent in image ⑩. Immediately after image ⑩, the specimen developed a crack through the thickness and the experiment was terminated. Similar to the previous example, a sudden partial load drop occurred right at failure as seen in image × as well as in Figure 3.7. Following the load drop, the specimen

was unloaded and detailed photographs were taken of the cracked region. Figure 3.9 shows two close up photographs of the crack, taken on either end of the crack. One can clearly see the discontinuity and the variation of deformation along the vertical direction within the images.

Post processing of the images taken of the deforming grid produced the strain path shown in Figure 3.6b. The trajectory, like that of the previous example, is nearly linear. Marked on the trajectory with the symbol ■ are the values corresponding to the load maxima. They correspond to values of $(\gamma,\varepsilon)_L$ = (0.187, 0.072) (Tables

Table 1). By contrast, the last point, marked with the symbol "×", came from the image taken at the termination of loading from the neighborhood of the tip of the crack. These measurements are designated as the "failure" values and are $(\gamma,\varepsilon)_f$ = (0.70, 0.330) (Table 2). The large magnitudes of these values further support the fact that most deformation takes place beyond the load maxima in the localizing zone. The equivalent plastic strain at failure was then evaluated as in Eq. (7) and the resulting e^p_{ef} = 0.510.

3.1.3 All Radial Results

Thirteen radial stress path experiments were performed where α was assigned eleven values between 0.125 and 2.5. The problem parameters are listed in Tables

Table 1. Figure 3.10a shows plots of the prescribed $\mathcal{T} - \Sigma$ paths. Figure 3.11a and Figure 3.11b show the measured shear stress-rotation and axial stress-displacement responses for 11 of the tests (two of the lower α values were repeated). The responses exhibit the expected trends, with the shear stress and rotation angle (ϕ) increasing as α decreases and the axial stress and elongation (δ) decreasing. Conversely, as α increases the axial stress and the test section elongation increase. Figure 3.10b show plots of the corresponding shear strain (γ) vs. the axial strain (ε). The trajectories are essentially linear with the amplitude of the undulations reflecting the accuracy of the estimates of deformation from the grid measurements.

Marked on all trajectories with a symbol "■" are the locations of the nominal stress maxima. All cases continued deforming well past the load maxima with the recorded nominal stress dropping and the deformation localizing in the manner described in the discussion around Figure 3.3 of Exp. 51. What is striking in all cases is the extent of local deformation that was recorded past the limit loads, where, in fact, local deformation is dominant as indicated in Figure 3.10b. In the majority of the experiments, the localization developed at mid-height of the test section. In two cases with larger values of α (2.0 and 2.5), deformation localized closer to one of the edges of the 0.400 in (10.2 mm) tall test section but clearly away from the radiused ends. With one exception, the test sections remained free of torsional buckling. In Exp. 50 with α = 0.125, small amplitude buckles appeared at a rotation (ϕ) of about 38°. The test was continued until failure, so the stress state at failure reported in Table 2 is influenced to some degree by the mild buckles that developed. In this case, the shear response remained essentially flat for most of the test and the quoted load maxima are best estimates.

Several of the tubes tested were sectioned in order to observe the through thickness deformation in the zone of failure. Figure 3.12 shows cross sectional images corresponding to α values of 0.25, 0.75, 1.0, 1.5 and 2.0 (1.0 represents a $\sigma \rightarrow \tau$ corner path, see Section 3.2). The majority of the sections showed little or no evidence of necking, and failure was nearly perpendicular to the tension direction. Exceptions are α = 0.25 and α = 2.0, where the failure was inclined and some amount of necking developed for α = 2.0. Necking, of course, violates the plane assumption made in our estimates of stress and deformation and contributes some error to the values quoted at failure in Table 2.

The final points of the $\gamma - \varepsilon$ trajectories in Figure 3.10b represent the strain measured adjacent to the failure zone at the end of the test. This data was also used to estimate the stresses and equivalent strain at failure using the methodology described in the previous section. The equivalent strain e^p_{ef} values, as defined in Eq. (7), are listed in Table 2 and plotted against the normalized mean stress (σ_m / σ_e) in Figure 3.13. The

failure strain grows monotonically as the mean stress decreases reaching values that exceed 1.0 at the lower values of mean stress considered. Thus, the "dip" for shear-dominant stress states, first reported in Bao and Wierzibcki [2004] for Al-2024-T351 and more recently in Beese *et al.* [2010] for Al-6061-T6, did not materialize in these results (it is worth mentioning that the majority of the results in these references came from sheet metal). Furthermore, the strain levels measured here are significantly higher than those in these works. A small dip in failure strain at higher shear stress states was also reported in Barsoum and Faleskog [2007] from biaxial tests on tubular specimens on two types of steels. These differences in trends and magnitude of e_{ef}^{p} may be due to differences in the materials analyzed including the effect of their processing, but quite possibly also due to differences in the testing procedures and in the ways the measurements of stresses and strains are performed.

3.2 SUMMARY OF RESULTS FROM CORNER $\mathcal{T}-\Sigma$ PATHS

As previously mentioned, four experiments were performed to investigate the path dependence of failure using the same aluminum tubular specimens. These experiments are very similar in nature to those presented by Korkolis and Kyriakides [2009]; however, the referenced experiments were performed using axial and hoop stresses with zero shear while the following experiments were performed using axial and shear stresses.

3.2.1 $\alpha = 1.0$

Experiments 33 and 34 provide an example of two corner paths that correspond with the radial path of α =1.0. Experiment 33 follows a $\tau \to \sigma$ path, while experiment 34 follows that of a $\sigma \to \tau$ path. The specimens were loaded using the method described

in Chapter 2.1 and the various parameters measured are given in Table 3. The stress paths corresponding to the two experiments can be seen in Figure 3.14a. The $\tau \to \sigma$ path is shown in red and the $\sigma \to \tau$ path in green, while the radial path is shown in blue. As mentioned in Chapter 2:, the preload in the corner paths was chosen to correspond to the stress at which the specimen failed in the corresponding radial path. Figure 3.15 shows the resultant $T - \phi$ and $\Sigma - \delta$ plots for both corner cases as well as the radial loading path. It is clear from these plots that the failure stresses exhibit some path dependence. In Figure 3.15a the shear stresses at failure are not very different. Figure 3.15b, on the other hand, shows that the axial stress at failure is strikingly higher for the $\tau \to \sigma$ path than for either of the other paths. Additionally, the tube had already plastically deformed once the initial shear stress level was established in the $\tau \to \sigma$ case, so the applied axial stress caused immediate hardening and plastic deformation. Also evident, is the much larger limit load present in the $\tau \to \sigma$ path, even though all three paths reach a limit load at very similar values of δ / L_g (approximately 0.045).

From the recorded images of the test section grid it was observed that the failure zones of the various corner paths showed similar deformation and localization behavior to that of the radial paths. The induced strain trajectories extracted from the time lapse photography, as plotted in Figure 3.14b, are very similar to one another and the failure strains display much less variation than the failure stresses. The measured stress and deformation variables at failure from the corner and radial paths are listed in Table 4. Additionally, the equivalent strain values at failure, e_{ef}^{p}, as defined in Eq. (7), were plotted against the normalized mean stress (σ_m / σ_e) in Figure 3.13. They are seen to follow a similar monotonically increasing trend to that of the radial results.

3.2.2 $\alpha = 1.5$

Experiments 49 and 45 are additional examples corner paths that correspond to the radial path of α =1.5. Experiment 49 follows a $\tau \to \sigma$ path, while experiment 45

follows that of a $\sigma \rightarrow \tau$ path. The experiments used the same procedures described above and the usual experimental measurements are given in Table 3. The stress paths corresponding to the two experiments can be seen in Figure 3.16a. The $\tau \rightarrow \sigma$ path is shown in red and the $\sigma \rightarrow \tau$ path in green, while the radial path is shown in blue. Figure 3.17 shows the resultant $\mathcal{T}-\phi$ and $\Sigma-\delta$ plots for both corner cases as well as the radial loading path. These plots show that there is not a significant difference in the failure stresses of the three paths. The limit loads, however, show more differences both in stress levels and also in terms of displacements and rotations than the previous case. In this instance, neither path has experienced any plastic deformation upon reaching the initial stress level; hence, the hardening behavior of the three paths is much more similar than the behavior seen in the α =1.0 corner paths. Although, much like the α =1.0 path for the $\tau \rightarrow \sigma$ case, the α =1.5 $\tau \rightarrow \sigma$ case shows yielding and hardening at a very low level of axial stress and a more precipitous drop in the axial stress after the limit load is reached. The three strain trajectories extracted from the time-lapse photography plotted in Figure 3.16b, are very similar to one another and so are failure strains. The measured stress and deformation variables at failure from the corner and radial paths are listed in Table 4. Additionally, the equivalent strain values at failure, e_{ef}^{p}, as defined in Eq. (7), were plotted against the normalized mean stress (σ_m / σ_e) in Figure 3.13. Once more, they form a tight group and fall in line with the radial path results.

Chapter 4: Grain Level Strain Estimates

The accuracy of the strain levels inside the localization zones reported this far is of course governed by the 0.03125 in (0.794 mm) size of the grid used in the test section. Ghahremaninezhad and Ravi-Chandar (G-RC—OFHC Copper [2011], Al-6061-T6 sheet [2012]) reported that in tensile tests to failure under uniaxial and nearly plane tension, localization took place at smaller scales than usual macroscopic measuring techniques can resolve. Using grain level deformations measured via optical microscopy, they showed that inside defuse necks that precede failure plastic deformation in narrow bands of material can significantly exceed macroscopically measured values. Here we report results from similar grain level measurements taken within the localization zone at the end of five of tests with α values of 0.25, 0.75, 1.0, 1.5 and 2.0.

4.1 Specimen Preparation

Small sectors (~20 mm wide) of the test section containing a visible crack tip were extracted using EDM. The aluminum specimens were each cleaned in an ultrasonic bath with ethyl alcohol for between five and ten minutes to minimize particles that could contaminate the polishing procedure and scratch the specimen. The electrochemically etched grid was assumed to be the most likely source of small particles; therefore, the grid was placed facing downwards in the bath so that it would knock any stray particles loose. After the ultrasonic bath, each piece was dried with pressurized air. Furthermore, after the bath, rubber gloves were used when handling the specimens to ensure that there were no additional particles introduced.

The specimens were individually mounted in epoxy to facilitate proper polishing of the grains. First, Allied High Tech Products Inc. 1.25 in diameter two-part mounting cups were coated in a mold release agent. Next, the specimens were individually mounted to the bottom of the cups using super glue to hold them in place during the epoxy pour. Each specimen was fixed such that the bottom face of the epoxy mold would be tangent

to the test section containing a crack. Then 20 g of Buehler EpoxiCure Resin was thoroughly mixed with 4 g of hardener (stirred for about five minutes) before being slowly poured into the container. Small pieces of paper were labeled in pencil (which would not be smeared by the epoxy as ink would) with the experiment name and stress ratio. These labels were submerged in the epoxy in order to keep track of each piece. Finally, the samples were placed in a vacuum chamber and were degassed for around 15 minutes. The epoxy was left to cure for 24 hours before polishing.

After the epoxy was allowed to cure, the specimens were ground and polished on a Buehler Ecomet 3 Variable Speed Grinder-Polisher by hand. The first pass on the wheel was a rough grind tangent to the concave test section to establish a properly flat and positioned face that included a crack tip. This pass used 240 grit wet sandpaper pads and took anywhere from 15 to 30 minutes, depending on the specimen. Next, finer grits were used to begin the polishing process. The table was run around 100 rpm with constant water running over the paper and pressure was applied by hand for each subsequent round of sanding. The specimens were moved around the platen in order to ensure that the face would remain level and no scratches were induced. The specimens were polished with four grits of sandpaper: 320, 600, 800, and finally 1200. Every grade of sandpaper was used for at least 90 seconds before moving on to the next step only when there was a consistent finish on the aluminum face. Between each grade of sandpaper, the specimens were cleaned in water before being dried with pressurized air. Additionally, starting with the 1200 grit paper, new gloves were used when switching polishing grades. Finally, the specimens were polished using felt cloths infused with 3 μm diamond paste saturated with oil (Allied High Tech Products Inc. GreenLube Polishing Lubricant) before being finished with a 1 μm diamond polish. It was found that the 3 μm step was most crucial in establishing a good finish on the aluminum face. The 3 μm polish, therefore, was not timed; rather, judgment was used for each case and each specimen would only proceed to the 1 μm step after making sure that no scratches or depressions were visible when examined under a bright light.

Several different etching techniques were tried from the ASM International article "Metallographic Technique for Nonferrous Metals and Special-Purpose Alloys" before a sufficient technique properly revealed the grain boundaries. The first attempts to reveal the grain boundaries were made using the Modified Keller's Reagent- 175 mL H_2O, 2 mL HF (48%), 3 mL HCl (conc), and 20 mL HNO_3. Examinations of the specimen lead to the conclusion that Modified Keller's Reagent was not a sufficient etchant for Al-6061-T6. Upon further research, this agrees with the conclusions of Vander Voort and Manilova's publication [2012], "Metallographic Etching of Aluminum and Its Alloys." The publication suggests that Weck's Reagent might yield better results.

The next attempt at etching the specimens utilized Weck's etchant- 4 g $KMnO_4$ and 1 g NaOH in 100 mL H_2O. A test specimen was submerged in a 2% NaOH solution for 1 minute to prepare the surface for Weck's etchant. Next, the sample was cleaned with water and dried before being submerged in Weck's etchant for about 5-10 s. The surface was examined under 200× magnification and faint grain boundaries were visible. Another test surface received longer submersion in Weck's etchant (10-15 s) and showed the grain boundaries more clearly. However, in the process of testing different etching techniques, one surface was submerged "out of order," meaning that it was submerged in the NaOH solution *after* being etched in Weck's etchant. The results from this happy accident revealed that the NaOH solution further enhanced the grain boundaries by dissolving a good deal of the green tint that Weck's etchant deposited on the surface of the grains. The resulting contrast between the grain boundaries and the grain bodies was much more pronounced and proved to be easier to analyze in subsequent steps. Thus, each of the surfaces polished from the five radial paths was prepared by submerging in NaOH, then Weck's etchant, and finally "cleaned" with another submersion in NaOH.

4.2 Optical Microscopy

Grain imaging was performed in a Nikon Eclipse optical microscope equipped with a digital camera with 200× magnification. The camera captured images 1280 × 960

pixels and was calibrated such that each pixel was 0.48 μm wide. About 20 overlapping micrographs were taken in the zone of interest and stitched together to form a mosaic micrograph using Microsoft *Image Composite Editor*. Figure 4.1 shows the composite in-plane image of a section of the undeformed tube with the vertical direction corresponding to the axis of the tube. The grain boundaries are well defined, and the grains appear nearly equi-axed with an average grain size of the order of 20 μm. The small dark spots dispersed in the grains are second phase particles such as the ones reported in G-RC [2012].

From these mosaic images, hundreds of grains could be analyzed using the "analyze particles" function of the NIH software *ImageJ*. The "analyze particles" feature can output a number of geometric properties of particles in a *thresholded* image. The mosaic micrographs were individually prepared for analysis using several filters in Adobe *Photoshop*. Each image required different settings, but the majority of them had their brightness and contrast settings adjusted before undergoing several bandpass filters to minimize gradients caused by the lighting of the microscope. Finally, a threshold filter would convert each image to binary black and white. The grain bodies would be converted to black and the grain boundaries to white, only then could the "analyze particles" feature in *ImageJ* work.

In order to sufficiently capture the grain level deformations, the "analyze particles" feature was set to output the equivalent ellipses and bounding rectangles of each particle. The "equivalent ellipse" feature fits an ellipse to each particle and outputs the lengths of the major and minor axes as well as the angle of the major axis with respect to horizontal. The bounding rectangle feature selects the smallest rectangle, aligned with the global horizontal and vertical axes, which will enclose each particle. Histograms of these geometries were generated for undeformed specimens as well as the five test specimens and used to estimate grain level strains as described below.

4.3 MICROSCOPIC STATISTICAL RESULTS

The following statistical analysis technique was developed based on the techniques described in G-RC [2012]. It involves comparing statistical values of grain measurements from undeformed reference specimens with those from deformed specimens. The results show that there may be another level of localization within macroscopically visible localized bands that can only be observed with microscopic analysis.

4.3.1 Undeformed Reference Statistics

Using *ImageJ*, 1723 of the undeformed grains in Figure 4.1 were fitted with equivalent ellipses. Statistical histograms of the major and minor axes lengths ($2a$ and $2b$) are shown in Figure 4.2a and Figure 4.2b respectively. Principal angle measurements of the ellipses showed the major axes to have a slight bias towards the tube drawing direction as seen in Figure 4.2c. The mean value of the major axis ($2\bar{a}$) is 32.6 μm (STD 21.9 μm) and of the minor axis ($2\bar{b}$) 20.1 μm (STD 12.3 μm). This is consistent with the relatively modest in-plane anisotropy reported in similar tubes in Korkolis *et al.* [2010]. An additional micrograph mosaic was produced from the undeformed specimen aligned through the thickness of the tube. The micrograph, seen in Figure 4.3, was used to analyze 3662 grains through the thickness of the tube. Figure 4.4a, Figure 4.4b and Figure 4.4c show histograms through the thickness of the tube. Here $2\bar{a}$ = 30.5 μm (STD 17.2 μm) and $2\bar{b}$ = 23.1 μm (STD 11.7 μm), again presumably a result of the drawing process. The principal angles of the through thickness grains showed even more of a bias towards the drawing direction.

4.3.2 Grain Strain Estimation Procedure for $\alpha = 0.75$

The procedure of extracting grain-level strains will be described through results for α = 0.75. Figure 4.5 shows a composite micrograph that contains on the right one of the tips of the crack formed. It is approximately 2400 μm wide by 1200 μm tall with the

vertical direction representing the axis of the tube. The grains are seen to be significantly sheared and stretched. Interestingly, the deformation is not uniform along the vertical direction as a narrow horizontal band of grains, from the cracked zone all the way across, are visibly more deformed. An approximately 300 μm tall band within this zone was arbitrarily chosen to develop a statistical estimate of the strain to failure. Colored in red are 652 grains that will be used for this purpose.

The chosen grains were fitted with equivalent ellipses using *ImageJ* and the lengths of the major and mirror axes ($2a'$ and $2b'$), the angles of rotation β', and the coordinates of the centroid of each ellipse were recorded. Figure 4.6a and Figure 4.6b show histograms of the lengths of the major and minor axes and Figure 4.6c a histogram of β'. They each have the following mean values and standard deviations:

$2\bar{a}'$= 50.9, STD = 26.1 μm; $2\bar{b}'$= 11.2, STD = 6.0 μm; $\bar{\beta}'$ = 59.5°, STD = 7.3°.

The numbers confirm that the deformation within this band is very large indeed. The mean in-plane dimensions of the undeformed grains ($2\bar{a}$, $2\bar{b}$) were subsequently used to estimate the principal stretches of each grain as follows:

$$\lambda_1 = \frac{a'}{\bar{a}}, \quad \lambda_2 = \frac{b'}{\bar{b}} \quad \text{and} \quad \lambda_3 = \frac{1}{\lambda_1 \lambda_2} \tag{8}$$

where incompressibility of deformations is assumed. The principal logarithmic strains e_i, $i = 1,3$ are evaluated as in (4e) and the equivalent plastic strain via (7). The average values of e_e^p from groups of 10 neighboring grains were then calculated and are plotted in Figure 4.7 against ξ, the distance of the centroid of each group from the crack tip. A total of 66 such points are included in the figure. The data has a mean value of equivalent strain ($\bar{e}_{eg}^p$) of 1.209 but exhibits significant scatter (SDV = 0.39), which, however, appears consistent along the length of the band analyzed. We are reminded that the undeformed grain dimensions exhibited significant variation, thus basing the values of λ_i on the mean values of these dimensions contributes to the scatter seen in Figure 4.7 (similar to that in G-RC, 2012). Included in the figure is the plastic equivalent strain at

failure from the macroscopic measurements reported in Section 3.1.3 (e^p_{ef} = 0.739). Interestingly, $\bar{e}^p_{eg}$ is 1.64 times the estimated macro strain.

As pointed out above, grain deformation is more localized in a relatively narrow zone of grains where failure eventually occurs. To illustrate this point we conducted similar grain strain measurements in two bands approximately 500 μm tall, the centerline of which is located 500 μm above and below the edges of the band shown in Figure 4.5 (see micrograph in Figure 4.8). In the top band, with a height of about 520 μm, 452 grains were analyzed (blue in color in Figure 4.8) and the equivalent strains are plotted in Figure 4.9a. Although the scatter seen in the data of the central band remains, the strain levels are significantly lower with some values being as low as the macroscopic measurement. The mean value of the strains, $\bar{e}^p_{eg}$, is 0.949 with a SDV of 0.54. The bottom band, which had a height of 580 μm, involved 535 grains (blue in color in Figure 4.8) and the resultant equivalent strains appear in Figure 4.9b. In this case too, the strain levels are lower than in the central band with $\bar{e}^p_{eg}$ = 0.957 and a SDV of 0.51. Thus, although both of these bands are within the zone used to calculate the macro strain using the grid, the mean strain levels are now only 29% higher than the macro measurement. This illustrates that within the zone of localization seen at the macro level (e.g., Figure 3.4) there exists a significant gradient of deformation. Clearly, this issue requires further consideration. Perhaps a more in depth statistical study of the grains could develop a new method for producing more rigorous results.

4.4 Grain Strain Results From Other Values of α

Similar grain-level strain estimates were generated in a similar fashion for four more of the test specimens and the results are summarized in Table 5 and specific descriptions are given in the proceeding sections. Clearly, as α increases, the difference

between the average grain strain and the macro measured value increase as does the scatter of the measured grain strains.

4.4.1 $\alpha = 0.25$

Using the micrograph shown in Figure 4.10, 709 grains were analyzed for experiment number 43 with a stress ratio of 0.25. The micrograph clearly shows a crack protruding into the section of the specimen analyzed from the left. The grains analyzed are highlighted in red and extend about 2000 μm to the right of the tip of the crack along the circumferential direction. The same techniques discussed for $\alpha = 0.75$ were used to produce histograms and a strain plot. Simple inspection of the grains in Figure 4.10 reveals even more severe deformation in this case and even more extreme aspect ratios than in the previous case. This is confirmed with Figure 4.11a, Figure 4.11b, and Figure 4.11c: the histograms of the major and minor axis lengths, as well as the major axis angle respectively. Statistical analysis provides the following mean and standard deviation values from the histograms:

$2\bar{a}'$ = 50.7, STD = 26.6 μm; $2\bar{b}'$ = 9.4, STD = 4.9 μm; $\bar{\beta}'$ = 63.6°, STD = 9.2°.

Calculating the average grain strains produces a microscopic $\bar{e}^{p}_{eg}$ = 1.302 and a SDV of 0.42, which is 25.4% higher than the calculated macroscopic strain. The grain strain plot can be seen in Figure 4.12 and shows all points of average grain strain to be significantly higher than the macroscopic strain level except for one outlier.

4.4.2 $\alpha = 1.0$

One $\sigma \rightarrow \tau$ corner path specimen from the $\alpha = 1.0$ set was selected to have its grains analyzed microscopically. Figure 4.13 shows the micrograph mosaic for the experiment chosen- No. 34. 740 grains were selected to generate equivalent strain values and equivalent ellipse histograms. These grains are highlighted in red color in Figure

4.13. Also visible in the figure is the crack tip protruding from the left about 200 μm into the image. Interestingly, the crack has bifurcated and shows both failure along grain boundaries and through grain bodies.

Statistical analysis confirmed that the grains selected showed similar trends to those analyzed in previous cases. Figure 4.14a, Figure 4.14b, and Figure 4.14c show the resulting histograms from the grain analysis that provide the following mean and standard deviation values:

$2\bar{a}'$ = 43.0, STD = 22.0 μm; $2\bar{b}'$ = 14.0, STD = 7.2 μm; $\bar{\beta}'$ = 50.7°, STD = 13.0°.

It can be readily seen that the average angle of rotation is decreasing as α increases. Calculating the average grain strains produces a microscopic $\bar{e}_{eg}^{p}$ = 1.042 and a SDV of 0.44, which is 90.5% higher than the calculated macroscopic strain. The grain strain plot can be seen in Figure 4.15 and shows a significant amount of scatter as is the trend with this analysis technique.

4.4.3 $\alpha = 1.5$

Experiment 36 with a stress ratio of 1.5 was also polished and analyzed in a similar manner. Figure 4.16 shows the micrograph image of the analyzed surface with 845 analyzed grains highlighted in red. Here it becomes more difficult to see the localized grains with the naked eye alone; for this reason, several different widths of bands were analyzed before settling on the final width after the results seemed to converge. Figure 4.17, parts a, b, and c show the histograms of the three geometries characterized from the 845 grains. The usual statistical analysis provides the following mean and standard deviation values from the histograms:

$2\bar{a}'$ = 43.5, STD = 24.0 μm; $2\bar{b}'$ = 16.4, STD = 9.0 μm; $\bar{\beta}'$ = 40.4°, STD = 14.4°.

Calculating the average grain strains produces a microscopic $\bar{e}_{eg}^{p}$ = 1.022 with a SDV of 0.47, which is 100% higher than the calculated macroscopic strain. The grain strain plot can be seen in Figure 4.18 and shows the usual scatter, but no outliers in the data.

4.4.4 $\alpha = 2.0$

Finally, experiment 39 was analyzed to capture the microscopic strains for a stress ratio of 2.0. Figure 4.19 shows the 989 grains highlighted in red that were analyzed for this case. This case shows the least grain rotation of all of the specimens analyzed and shows significant standard deviation as reported by the histograms in parts a, b, and c of Figure 4.20. Statistical analysis of the grains gives the following mean and standard deviation values:

$2\bar{a}'$ = 37.1, STD = 20.6 μm; $2\bar{b}'$ = 15.5, STD = 8.6 μm; $\bar{\beta}'$ = 30.9°, STD = 20.2°.

The larger standard deviations show up when calculating the average grain strains as $\bar{e}^{p}_{eg}$ = 0.993 and the SDV is 0.48. Here, like the case of α = 1.5, the microscopic strain is calculated to be over twice the macroscopically measured equivalent plastic strain. Figure 4.21 shows the final grain strain plot. The figure shows a fairly tight grouping of points near the tip of the crack (as ξ approaches zero), but the scatter is very large beginning around 400 μm from the crack tip. It can be safely assumed that the microscopic strain levels are higher than those observable using macroscopic techniques; however, the statistical scatter requires a much more thorough study to narrow the error band represented by the scatter of the data points.

Chapter 5: Summary and Conclusions

The plastic deformation and failure of Al-6061-T6 tubes under radial and corner paths of tension and torsion was investigated experimentally using a custom specimen design and test set-up. The set-up involves a two-inch diameter (50 mm) tube with a 0.125-inch (3.2 mm) wall into which a test section approximately 0.6-inch wide (15 mm) with a wall thickness of about 0.040 in (1.0 mm) is machined. For the radial experiments, the specimen is loaded under rotation control and a feedback loop keeps the axial load at a constant ratio to the induced torque. The test section deformation is established from a fine square grid (0.031 in— 0.79 mm) etched on the surface of the tube that is monitored by a computer operated digital camera triggered at intervals of a few seconds.

A shear dominated loading regime was considered through thirteen radial path experiments with stress ratios (σ/τ) α ranging from 0.125 to 2.5 as well as four corner stress paths corresponding to radial α values of 1.0 and 1.5. Typically, the test section deformed uniformly, developing significant shear and axial strains. The torque-rotation and axial-force displacement responses gradually lost stiffness, reaching maximum values. At this point, deformation started to localize, usually in a narrow zone that was of the order of the wall thickness, in the central part of the test section. Localized deformation continued, reaching quite significant levels, while the loads gradually decreased. At some point, a through-thickness crack appeared in the localized zone that covered part of the circumference (arrested by the stiff set up used). The test was terminated, the specimen was unloaded, and the deformation in the neighborhood of the crack was examined using a low magnification microscope. In most of the experiments the etched grid lines (depth ~ 12 μm) provided enough of a stress riser to trigger the localization.

The in-plane principal stretches were estimated using discrete images of the deformed grid taken in the neighborhood of the crack tips during the test, while the through-thickness stretch came from incompressibility. The last set of measurements of

the principal strain ratios of each test were used to estimate the equivalent plastic strain "at failure."

The results from the four corner path experiments show that the $\varepsilon - \gamma$ paths were not substantially different than the corresponding paths from the radial experiments. Additionally, the failure strains from the corner paths were in agreement with those from the radial paths. However, the $\tau \to \sigma$ corner paths showed substantially higher stress values in the $\Sigma - \delta$ plots compared to the other two loading paths for each case.

The true shear and axial stresses were estimated from the measured loads using the through-thickness stress ratio and by assuming the deformation to be planar. The hoop stress was estimated by assuming the circumference to be inextensible. The relevant stress invariants at failure were calculated from the stress levels at the onset of failure.

In summary, unlike previous efforts to estimate the conditions at failure under shear dominated loadings, in the present study both the deformation and stresses were established strictly from experimental measurement, without reverting to any constitutive model. Constitutive modeling, including characterization of the anisotropy in the tubes used, is presently in progress. This is a necessary first step for any effort to numerically simulate the radial path experiments. The following observations can be made from the results:

(a) The engineering strains were found to trace nearly linear trajectories in the $\varepsilon - \gamma$ plane for all cases. The extent to which these trajectories deviate from linearity is a gage of the error in the discrete measurements using the grid as gage length.

(b) As the mean stress decreased, the strain at failure showed a monotonic increase, a result that is in contrast with previously reported results for Al alloys. Furthermore, the values of the reported failure strains are significantly larger than previously reported values. These differences point out that establishing the onset of failure experimentally is very challenging and that experimental set-ups and diagnostic methods used can have significant influence on the results. Furthermore, interpretation of such results can be further complicated when indirect methods of estimating the stresses

and deformations at failure based on incomplete constitutive characterization are used. It is noted that we have not yet explored the influence of J_3 on the failure strain.

Clearly, the accuracy of the deformed grid method used to estimate the deformation inside the localization zone is influenced by the size of the grid (0.79 mm). This is alleviated to some degree by the fact that the width of the localization zone was of the order of the wall thickness (1.0 mm) while that of the grid was somewhat smaller. At higher values of α, the zone of localization tends to develop some through thickness necking. This violates the planar deformation assumptions made, further reducing the accuracy of the estimated stresses and strains at failure.

For several of the failed tubes, a section that contained a crack tip was removed from the test section, was polished and etched to enable optical microscope observations of the deformation at the grain level in the neighborhood of failure. Statistical estimates of the grain-level strains revealed that within the macroscopically identified localization zone there exists a gradient in the deformation; a zone spanning the crack approximately 300 μm wide was found to have deformed to strain levels that were between 25% and 100% higher than the average values estimated using the grid measurements. This indicates that localization also occurs at a smaller scale than hitherto understood (see also G-RC, 2012). Additional analysis was performed using SEM and is reported in Haltom *et al.* [2012].

Tables

Table 1: Main parameters for tension-torsion radial experiments.

Exp. No.	Tube No.	α	D in (mm)	t in (mm)	Ξ_o %	$\Sigma_{\max}$ ksi (MPa)	$\mathcal{T}_{\max}$ ksi (MPa)	ε_L %	γ_L %
47	DC13	0.125	1.9678 (49.98)	0.0395 (1.01)	0.8	3.49 (24.1)	28.64 (197.5)	1.96	68.53
50*	DC14	0.125	1.9670 (49.96)	0.0404 (1.03)	0.6	3.57 (24.6)	28.11 (193.9)	3.91	82.52
43	DC13	0.25	1.9682 (49.99)	0.0402 (1.02)	0.3	7.04 (48.6)	28.05 (193.4)	4.67	70.41
44	DC13	0.375	1.9669 (49.96)	0.0393 (1.00)	0.5	10.32 (71.2)	27.52 (189.8)	4.17	50.00
40	DC13	0.5	1.9683 (49.99)	0.0385 (0.98)	1.0	13.46 (92.8)	26.86 (185.2)	4.89	32.00
51	DC14	0.5	1.9679 (49.98)	0.0402 (1.02)	0.7	13.16 (90.8)	26.19 (180.6)	3.42	36.45
38	DC13	0.75	1.9684 (49.99)	0.0377 (0.96)	0.9	19.47 (134.3)	26.07 (179.8)	4.87	28.83
30	DC12	1.0	1.9680 (49.99)	0.0379 (0.96)	2.0	24.47 (168.7)	24.47 (168.7)	4.98	22.19
35	DC13	1.25	1.9681 (49.99)	0.0376 (0.96)	0.9	28.92 (199.4)	23.17 (159.8)	6.93	23.21
36	DC13	1.5	1.9683 (49.99)	0.038 (0.97)	0.7	32.85 (226.6)	21.77 (150.1)	7.17	18.71
37	DC13	1.75	1.9682 (49.99)	0.0384 (0.98)	0.8	35.55 (245.2)	20.11 (138.7)	6.33	13.15
39	DC13	2.0	1.9670 (49.96)	0.0388 (0.99)	0.6	37.60 (259.3)	18.61 (128.3)	6.34	10.90
41	DC13	2.5	1.9684 (50.00)	0.0383 (0.97)	1.4	41.21 (284.2)	16.43 (113.3)	8.09	11.11

* As mentioned in Section 3.1.3, mild buckling was observed

$$\Sigma = \alpha \mathcal{T}, \quad \Xi_o = \frac{t_{\max} - t_{\min}}{t_{\max} + t_{\min}}$$

Table 2: Stress and deformation variables at failure for radial stress paths.

Exp. No.	α	Σ_f ksi (MPa)	$\mathcal{T}_f$ ksi (MPa)	ε_f %	γ_f %	σ_f ksi (MPa)	τ_f ksi (MPa)	σ_{ef} ksi (MPa)	σ_{mf} ksi (MPa)	$\frac{\sigma_{mf}}{\sigma_{ef}}$	$\bar{\theta}$	ω	e_{ef}^p
47	0.125	3.44 (23.7)	28.53 (196.8)	3.09	110.00	3.38 (23.3)	28.86 (199.0)	50.07 (345.3)	1.69 (11.7)	0.03	0.10	0.9771	0.992
50*	0.125	3.47 (23.9)	27.39 (188.9)	5.51	122.00	3.48 (24.0)	28.87 (199.1)	50.09 (345.4)	1.74 (12.0)	0.03	0.10	0.9757	1.268
43	0.25	7.01 (48.3)	27.90 (192.4)	7.24	113.00	7.56 (52.1)	30.11 (207.7)	52.56 (362.5)	3.78 (26.1)	0.07	0.21	0.8984	1.038
44	0.375	10.09 (69.6)	26.96 (185.9)	9.10	105.00	11.13 (76.8)	29.77 (205.3)	52.45 (361.7)	5.57 (38.4)	0.11	0.31	0.7870	0.883
40	0.5	13.26 (91.4)	26.46 (182.5)	14.42	96.00	14.97 (103.2)	29.54 (203.7)	52.78 (364.0)	7.49 (51.7)	0.14	0.41	0.6404	0.739
51	0.5	12.89 (88.9)	25.70 (177.2)	11.86	110.00	14.31 (98.7)	28.52 (196.7)	50.93 (351.2)	7.16 (49.4)	0.14	0.41	0.6463	0.968
38	0.75	19.13 (131.9)	25.60 (176.6)	14.92	96.00	22.02 (151.9)	29.48 (203.3)	54.50 (375.9)	11.01 (75.9)	0.20	0.59	0.3637	0.739
30	1.0	23.63 (163.0)	23.67 (163.2)	20.37	87.00	28.10 (193.8)	28.14 (194.1)	54.48 (375.7)	14.05 (96.9)	0.26	0.76	0.1369	0.631
35	1.25	27.40 (189.0)	21.93 (151.2)	24.55	70.95	34.09 (235.1)	27.29 (188.2)	55.74 (384.4)	17.05 (117.6)	0.31	0.91	0.0198	0.501
36	1.5	31.25 (215.5)	20.70 (142.8)	32.98	70.00	39.71 (273.9)	26.30 (181.4)	57.07 (393.6)	19.85 (136.9)	0.35	0.95	0.0058	0.510
37	1.75	33.25 (229.3)	18.80 (129.7)	34.51	61.00	42.67 (294.3)	24.12 (166.3)	55.77 (384.6)	21.34 (147.2)	0.38	0.83	0.0675	0.458
39	2.0	34.64 (238.9)	17.13 (118.1)	33.54	52.00	44.47 (306.7)	21.99 (151.7)	54.16 (373.5)	22.24 (153.4)	0.41	0.73	0.1658	0.409
41	2.5	36.80 (253.8)	14.65 (101.0)	39.52	43.00	48.66 (335.6)	19.38 (133.7)	53.87 (371.5)	24.33 (167.8)	0.45	0.58	0.3779	0.399

Table 3: Main parameters for tension-torsion corner stress path experiments.

Exp. No.	Tube No.	α	D in (mm)	t in (mm)	Ξ_o %	$\Sigma_{\max}$ ksi (MPa)	$\mathcal{T}_{\max}$ ksi (MPa)	ε_L %	γ_L %
33	DC13	1.0 τ→σ	1.9675 (49.97)	0.0385 (0.98)	0.6	30.60 (210.98)	23.35 (160.99)	5.12	20.86
34	DC13	1.0 σ→τ	1.9682 (49.99)	0.0383 (0.97)	1.0	24.02 (165.61)	24.76 (170.71)	8.84	28.57
30	DC12	1.0	1.9680 (49.99)	0.0379 (0.96)	2.0	24.47 (168.7)	24.47 (168.7)	4.98	22.19
49	DC14	1.5 τ→σ	1.9675 (49.97)	0.0382 (0.97)	0.6	34.69 (239.18)	20.43 (140.86)	7.51	18.67
45	DC13	1.5 σ→τ	1.9660 (49.94)	0.0382 (0.97)	1.0	30.97 (213.53)	22.43 (154.65)	6.04	17.33
36	DC13	1.5	1.9683 (49.99)	0.038 (0.97)	0.7	32.85 (226.6)	21.77 (150.1)	7.17	18.71

$$\Xi_o = \frac{t_{\max} - t_{\min}}{t_{\max} + t_{\min}}$$

Table 4: Stress and deformation variables at failure for corner stress paths.

Exp. No.	α	Σ_f ksi (MPa)	$\mathcal{T}_f$ ksi (MPa)	ε_f %	γ_f %	σ_f ksi (MPa)	τ_f ksi (MPa)	σ_{ef} ksi (MPa)	σ_{mf} ksi (MPa)	$\frac{\sigma_{mf}}{\sigma_{ef}}$	$\bar{\theta}$	ω	e_{ef}^{p}
33	1.0 τ→σ	27.67 (190.78)	23.31 (160.72)	21.41	78.50	32.82 (226.29)	27.58 (190.16)	55.59 (383.28)	16.41 (113.14)	0.30	0.88	0.0373	0.550
34	1.0 σ→τ	24.01 (165.54)	24.03 (165.68)	22.22	78.00	28.90 (199.26)	28.92 (199.40)	55.99 (386.04)	14.45 (99.63)	0.26	0.76	0.1365	0.547
30	1.0	23.63 (163.0)	23.67 (163.2)	20.37	87.00	28.10 (193.8)	28.14 (194.1)	54.48 (375.7)	14.05 (96.9)	0.26	0.76	0.1369	0.631
49	1.5 τ→σ	29.82 (205.60)	20.40 (140.65)	37.23	85.00	39.60 (273.03)	27.09 (186.78)	58.12 (400.72)	19.80 (136.52)	0.34	0.98	0.0048	0.637
45	1.5 σ→τ	30.95 (213.39)	20.62 (142.17)	26.72	71.10	39.10 (269.59)	26.05 (179.61)	56.42 (389.00)	19.55 (134.79)	0.35	0.96	0.0015	0.508
36	1.5	31.25 (215.5)	20.70 (142.8)	32.98	70.00	39.71 (273.9)	26.30 (181.4)	57.07 (393.6)	19.85 (136.9)	0.35	0.95	0.0058	0.510

Table 5: Summary of grain-level strain measurements and corresponding macro-level values measured.

Exp. No.	α	No. Grains	$\bar{e}_{eg}$ (SDV)	e_{ef}
43	0.25	709	1.302 (0.42)	1.038
38	0.75	652	1.209 (0.39)	0.739
34	1.0 $\sigma \rightarrow \tau$	740	1.042 (0.44)	0.547
36	1.5	845	1.022 (0.47)	0.510
39	2.0	989	0.993 (0.48)	0.409

Figures

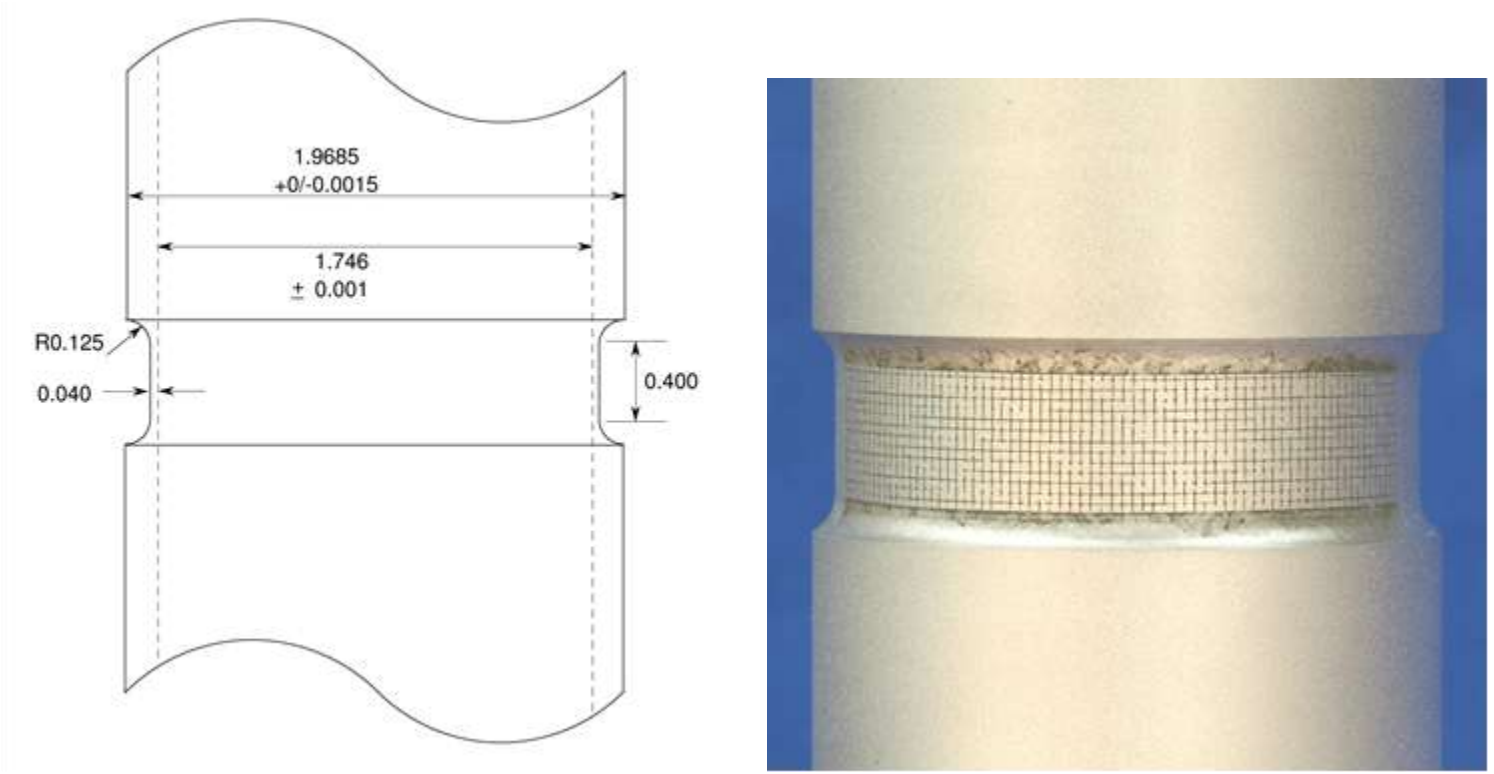

(a) (b)

Figure 2.1: Tubular specimen used in the tension-torsion radial stress path experiments. (a) Scaled drawing showing the test section and (b) photograph showing the square grid placed on the test section (dim. in inches — 1in = 25.4 mm).

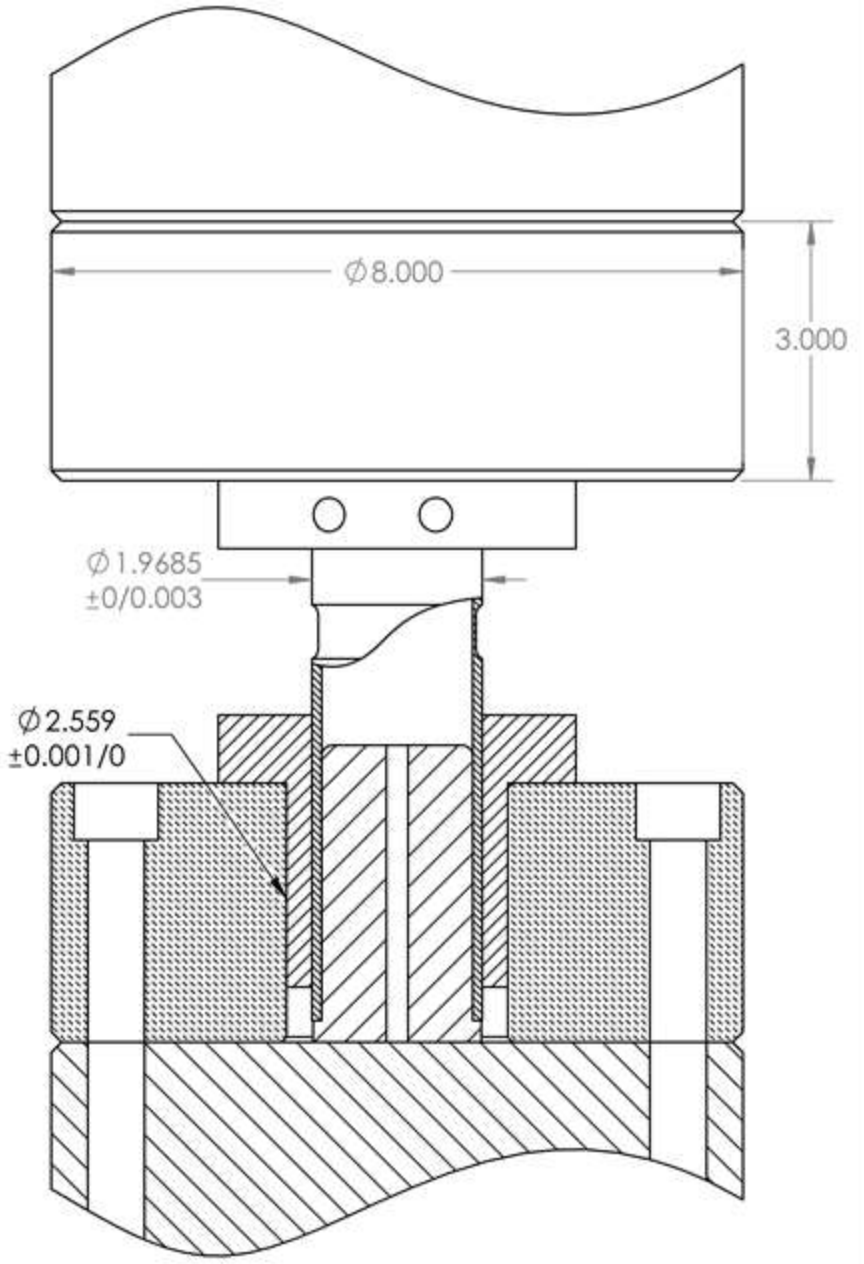

Figure 2.2: Scaled drawing of the gripping mechanism used to mount the specimen on to the axial-torsional testing machine (dim. in inches — 1 in = 25.4 mm).

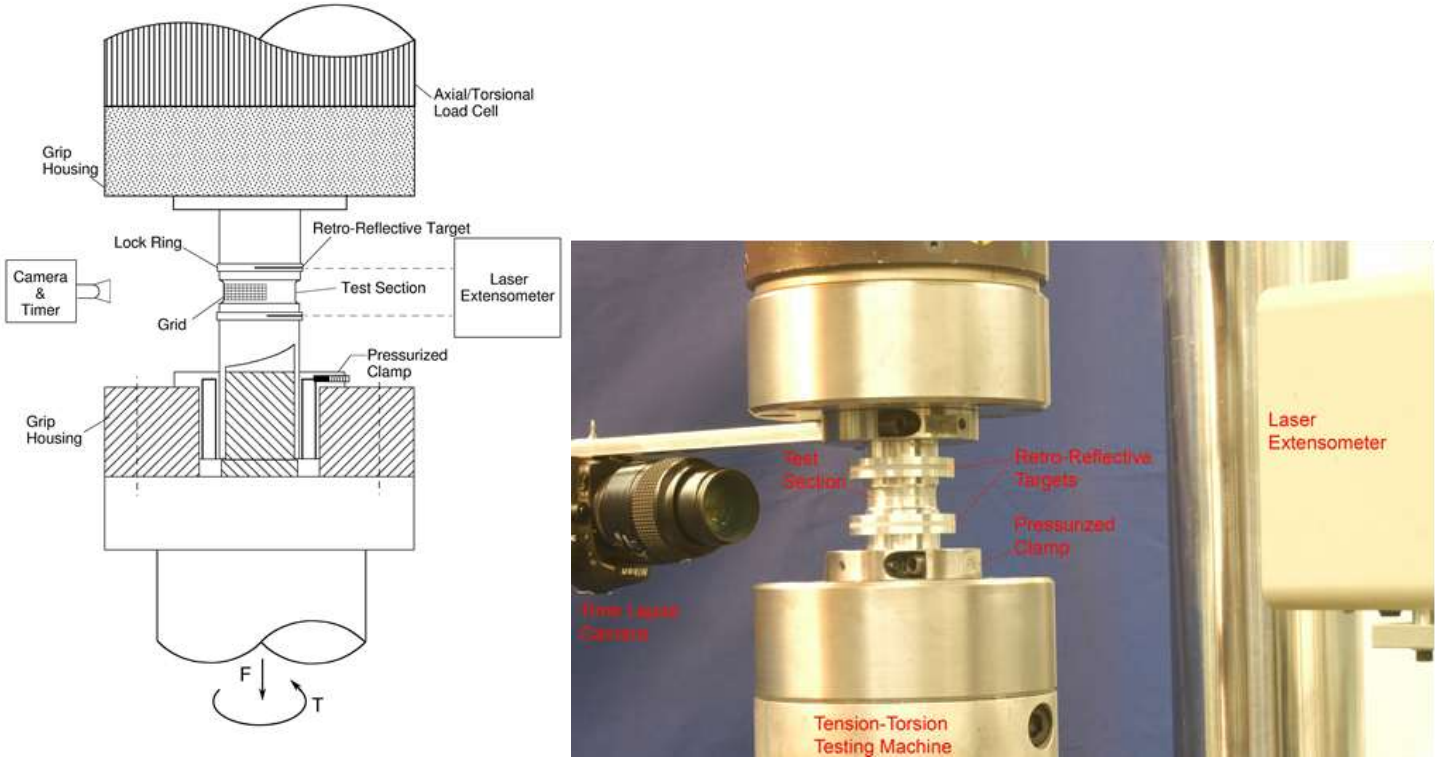

(a) (b)

Figure 2.3: Experimental set up: (a) Scaled drawing and components and (b) photograph.

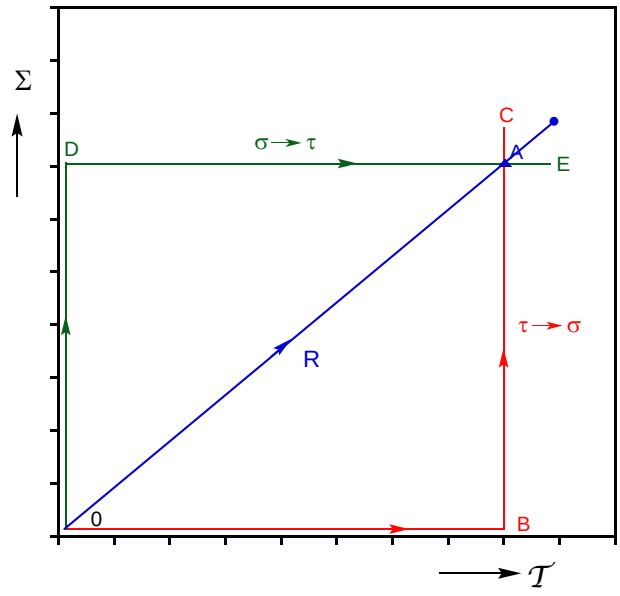

Figure 2.4: Schematic of corner stress paths with radial path as well.

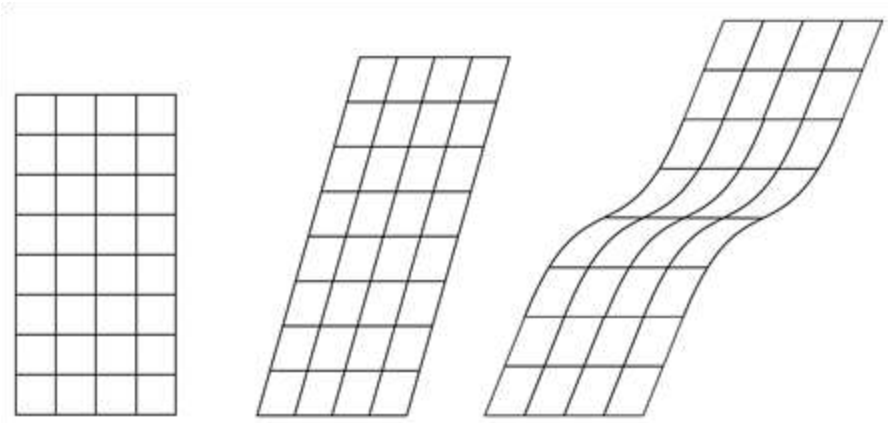

(a) (b) (c)

Figure 2.5: Schematic showing (a) the initial grid, (b) uniformly deformed and (c) localized.

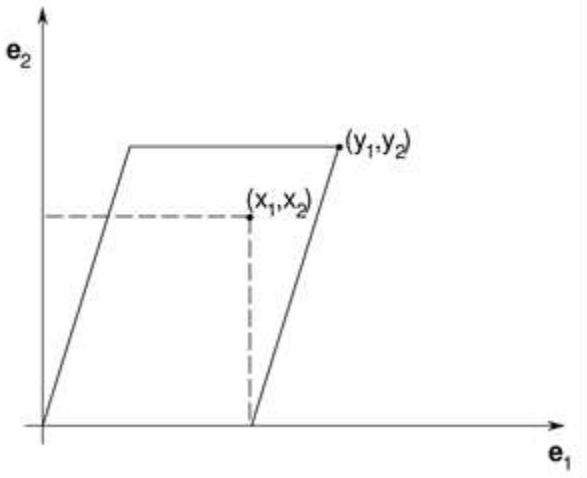

Figure 2.6: Coordinates of the initially square grid and of the idealized deformed configuration resulting from combined tension-torsion.

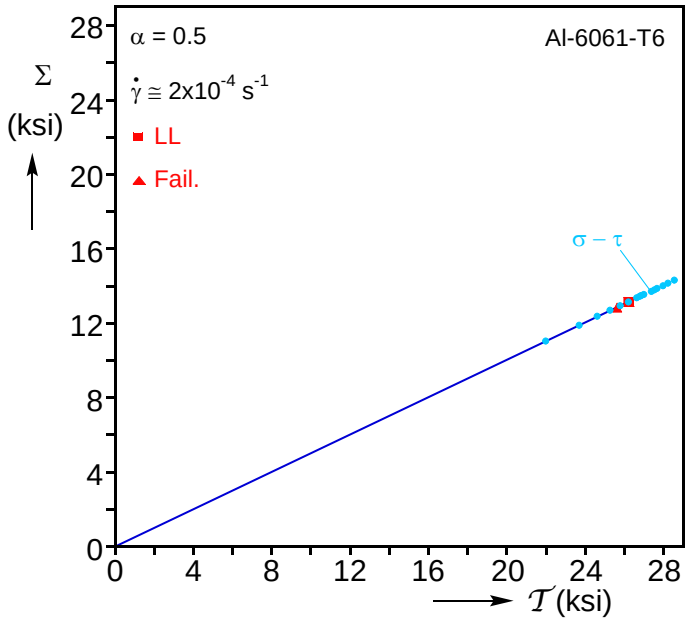

(a)

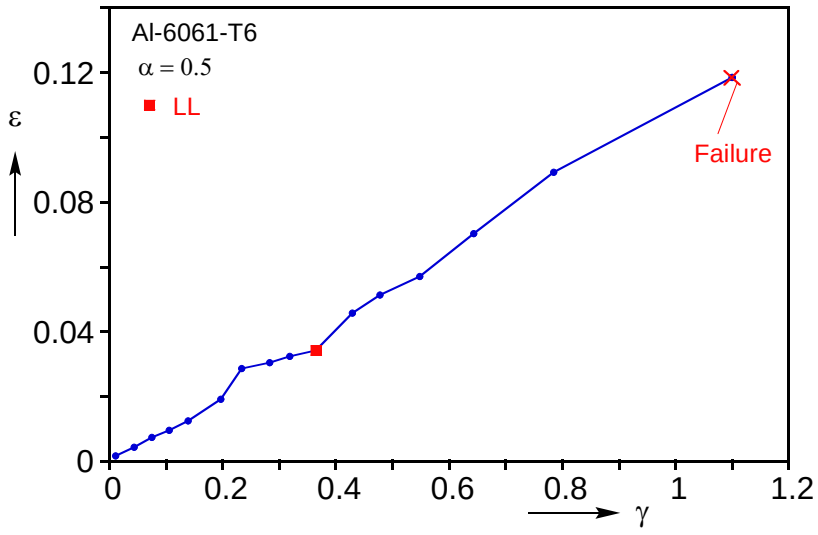

(b)

Figure 3.1: (a) Radial Σ - $\mathcal{T}$ stress path prescribed for $\alpha = 0.5$ including the stress maxima and the values at failure. Bullets represent corresponding true stress values. (b) Induced nominal strain path—values extracted from deformed grid.

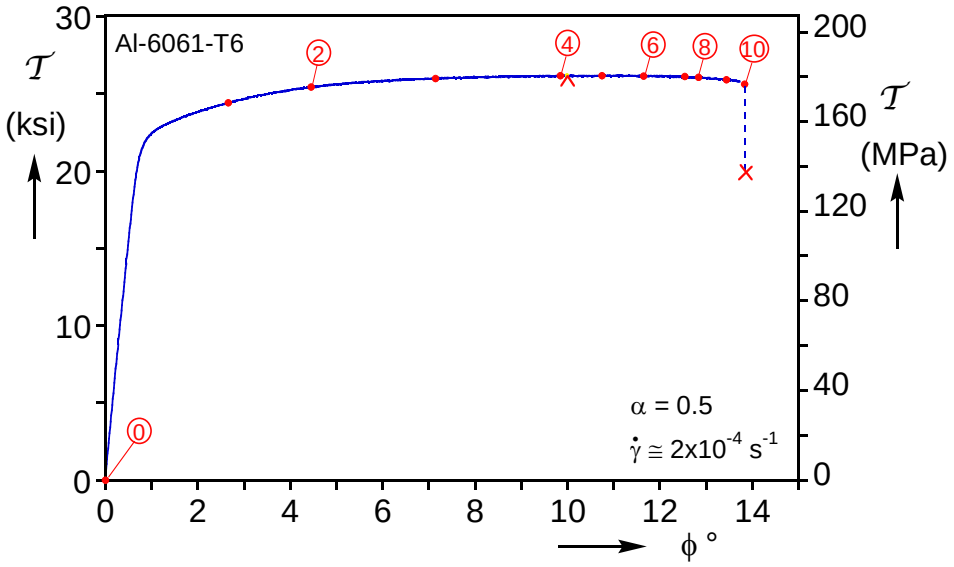

(a)

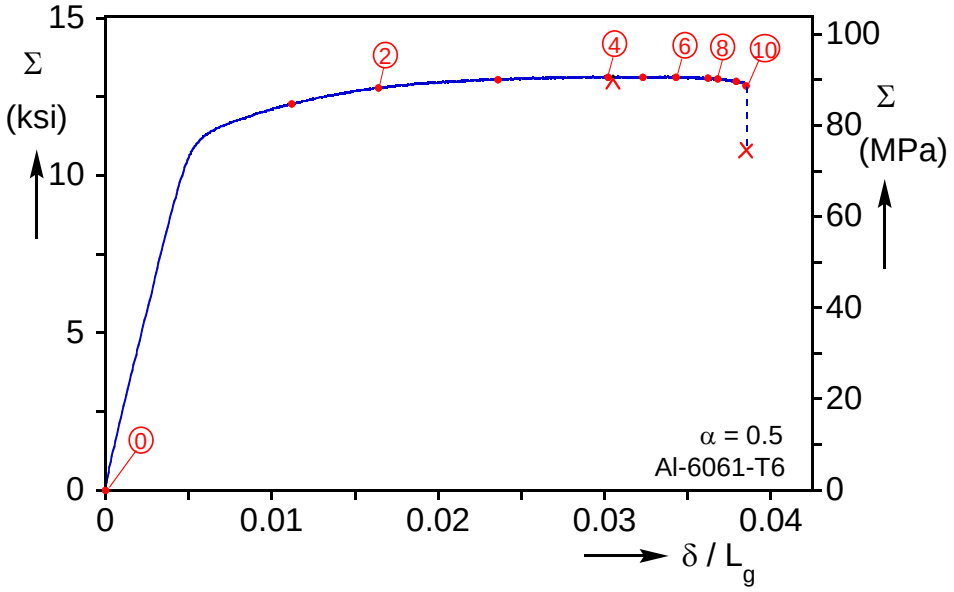

(b)

Figure 3.2: (a) Nominal shear stress-rotation and (b) axial stress-displacement responses for $\alpha = 0.5$.

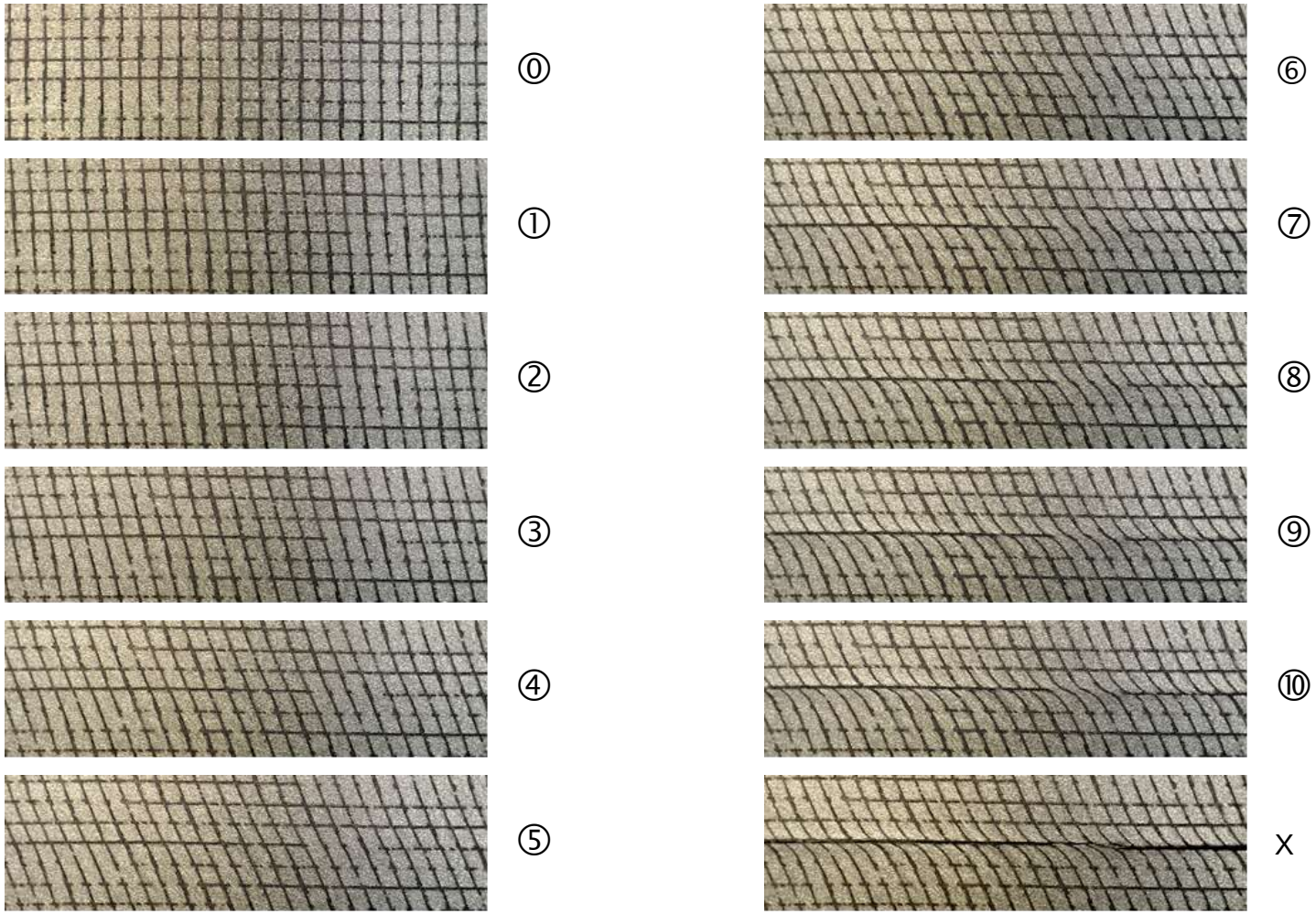

Figure 3.3: Sequence of images corresponding to numbered bullets on the responses in Figure 3.2 showing a zone of the deforming grid where localization and eventually failure takes place for $\alpha = 0.5$.

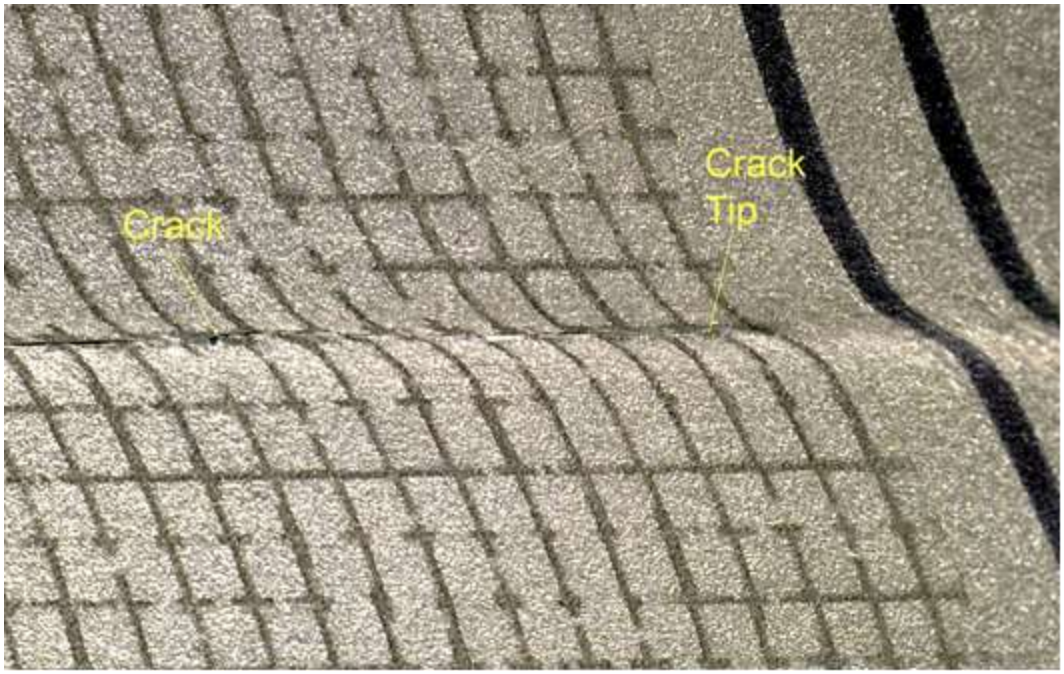

Figure 3.4: Expanded image of the grid taken at the end of the $\alpha = 0.5$ test showing the localized zone, the crack and its tip.

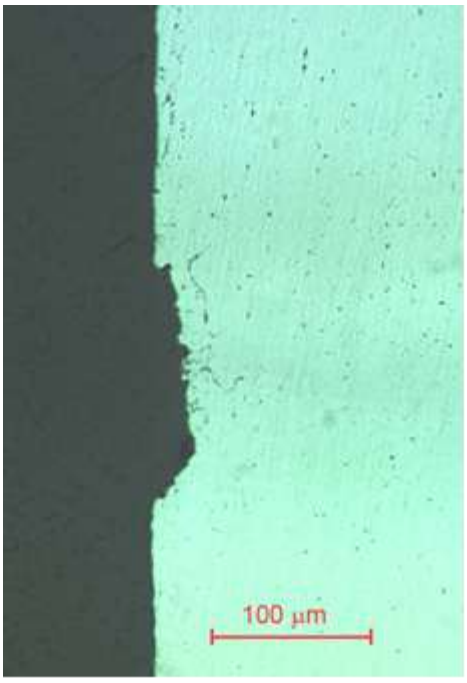

Figure 3.5: Micrograph showing a cross sectional view of one of the test section grid lines introduced by electro-etching.

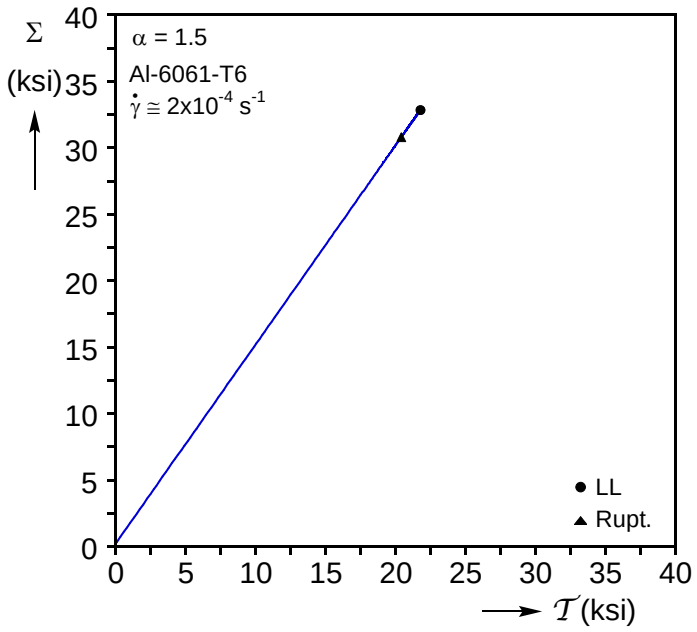

(a)

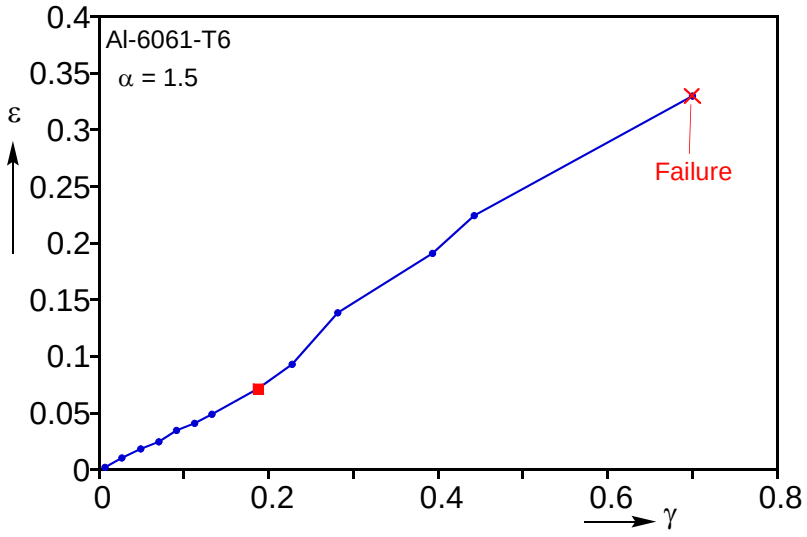

(b)

Figure 3.6: (a) Radial Σ - $\mathcal{T}$ stress path prescribed for $\alpha = 1.5$ including the stress maxima and the values at failure. Bullets represent corresponding true stress values. (b) Induced nominal strain path.

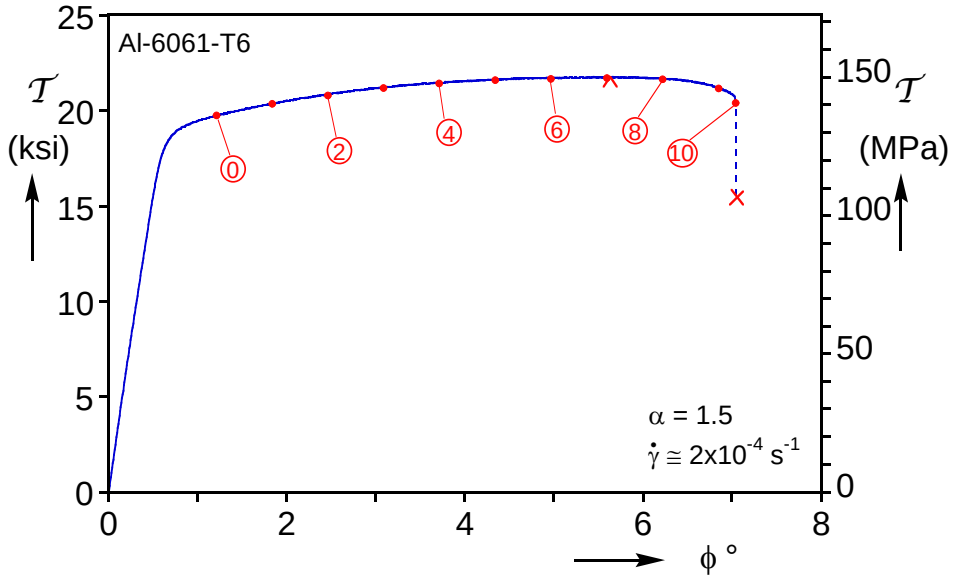

(a)

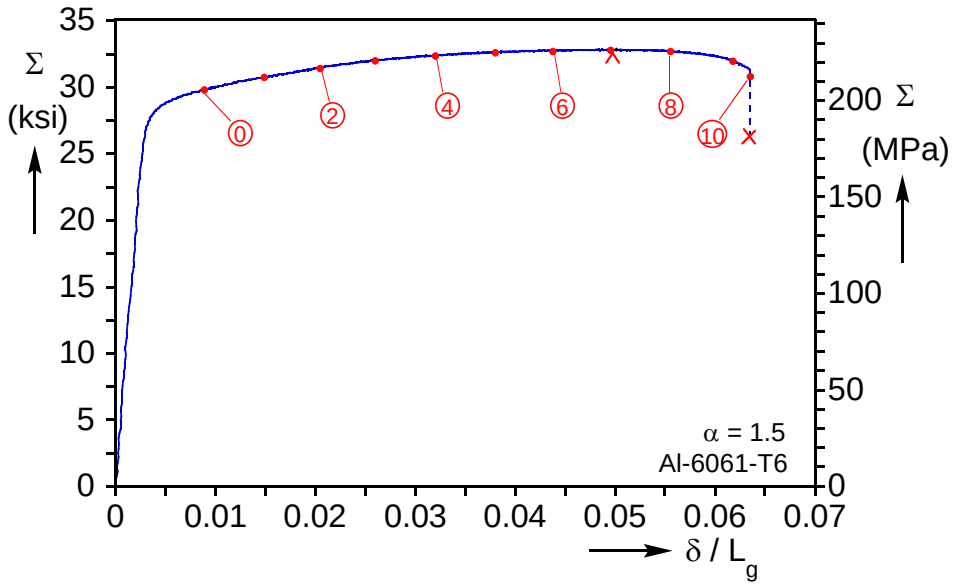

(b)

Figure 3.7: (a) Nominal shear stress-rotation and (b) axial stress-displacement responses for $\alpha = 1.5$.

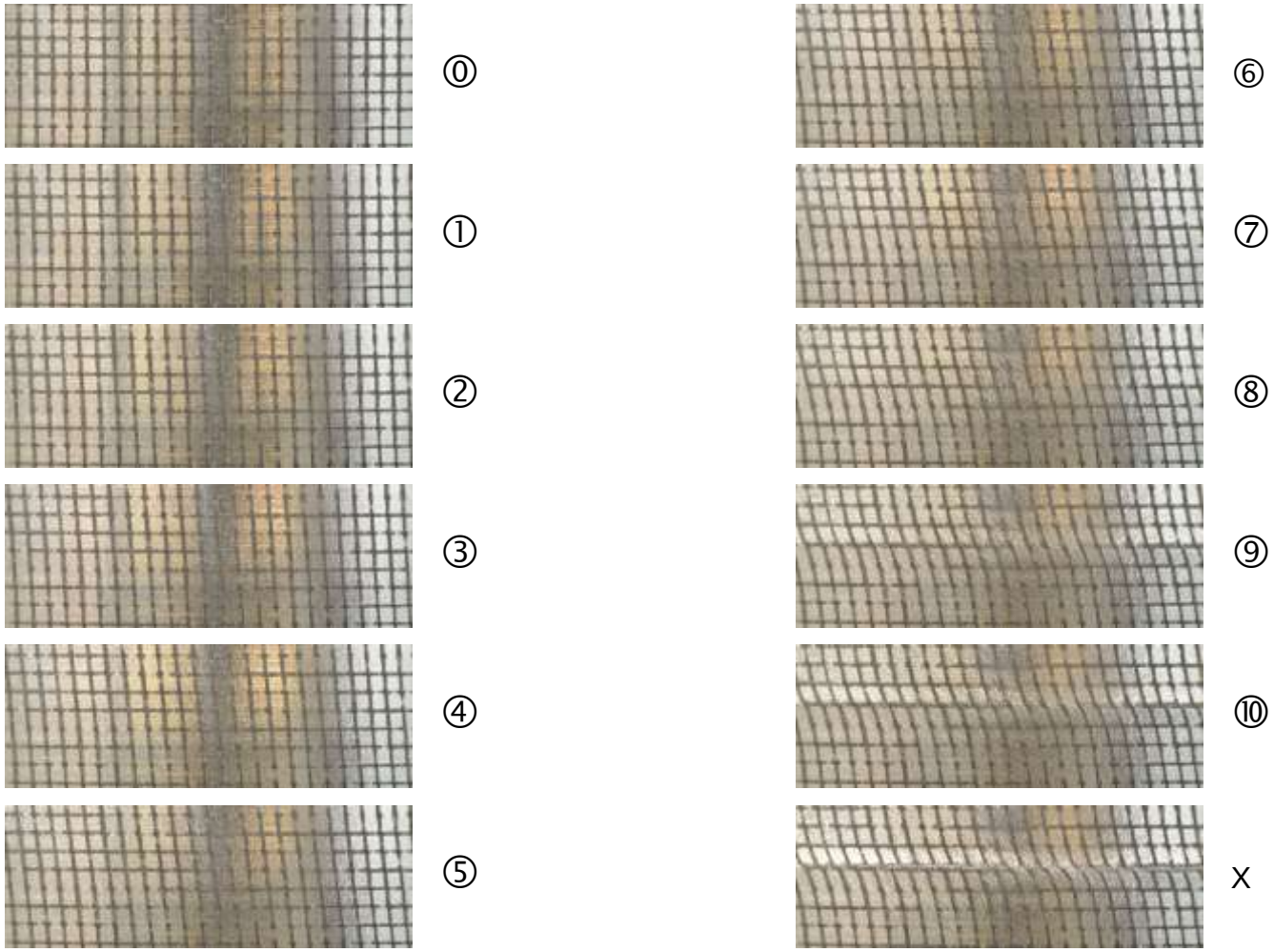

Figure 3.8: Sequence of images corresponding to numbered bullets on the responses in Figure 3.7 showing a zone of the deforming grid where localization and eventually failure takes place for α = 1.5.

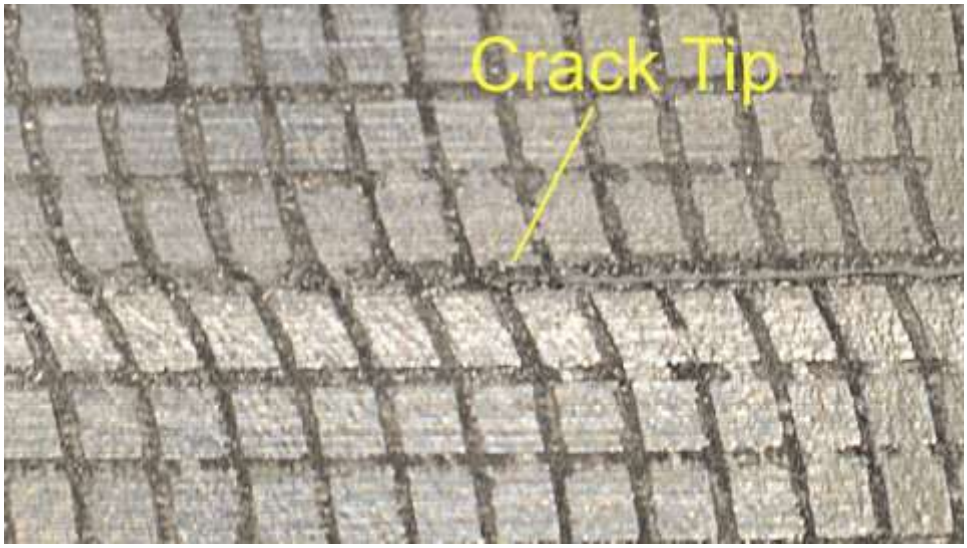

(a)

(b)

Figure 3.9: Expanded images of the grid taken at the end of the α = 1.5 test showing the localized zone and crack extending from the right (a) and from the left (b).

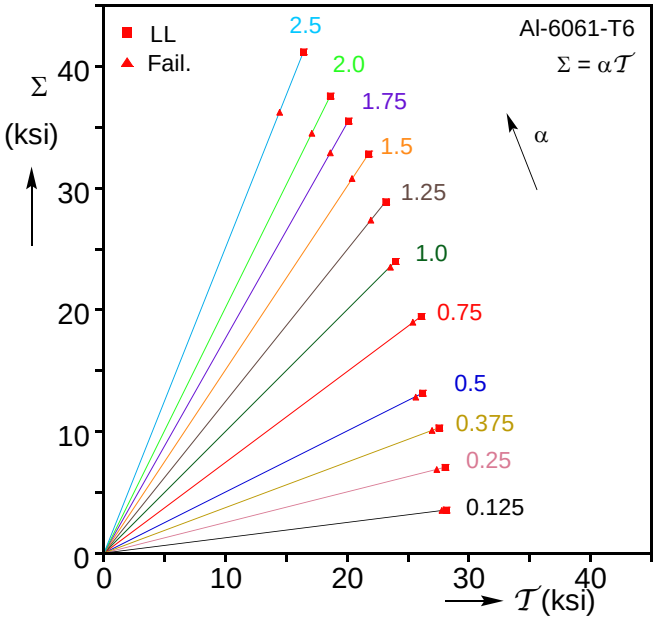

(a)

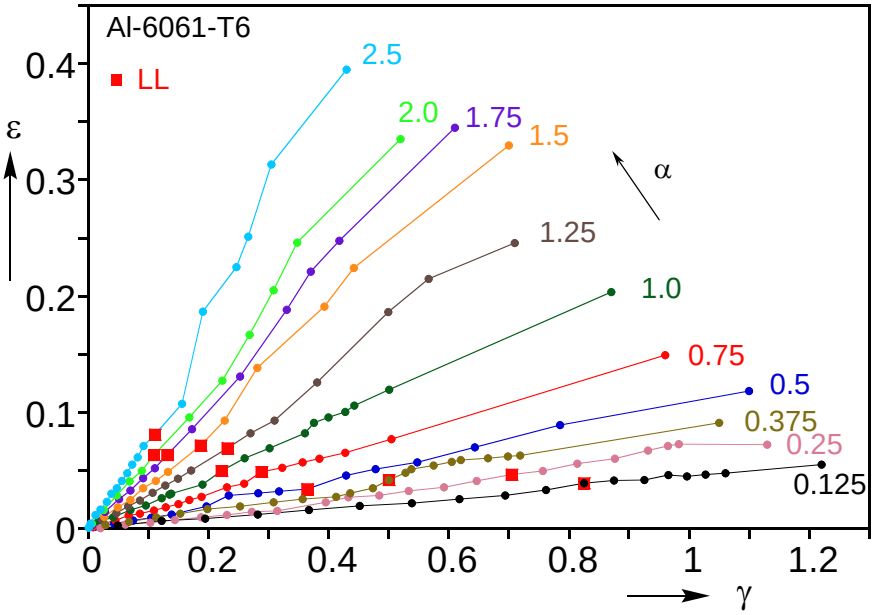

(b)

Figure 3.10: Eleven radial Σ - $\mathcal{T}$ stress path prescribed for various values of α; marked are the stress maxima and the values at failure. (b) Induced nominal strain paths.

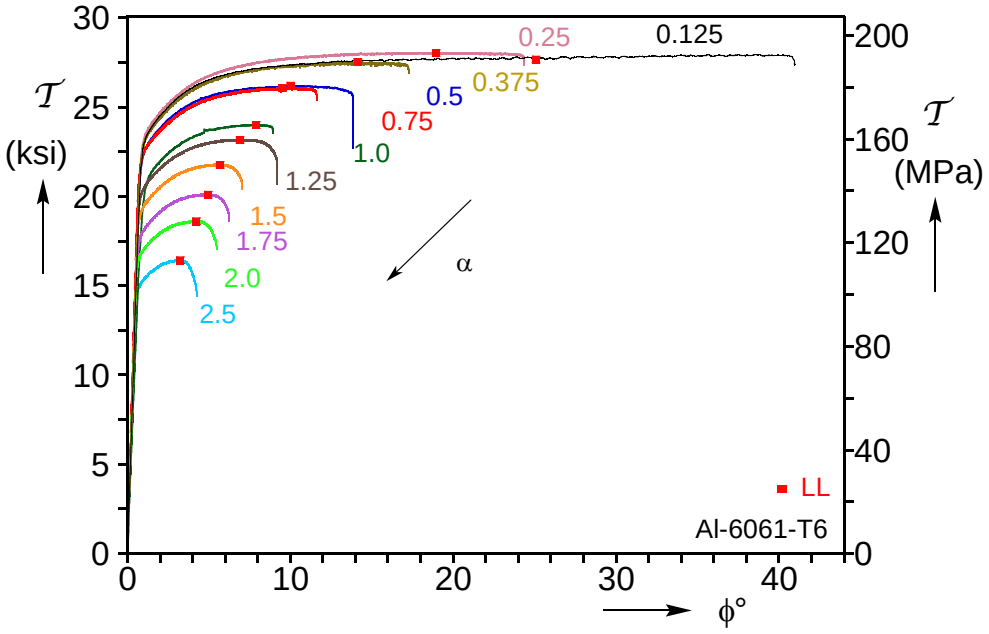

(a)

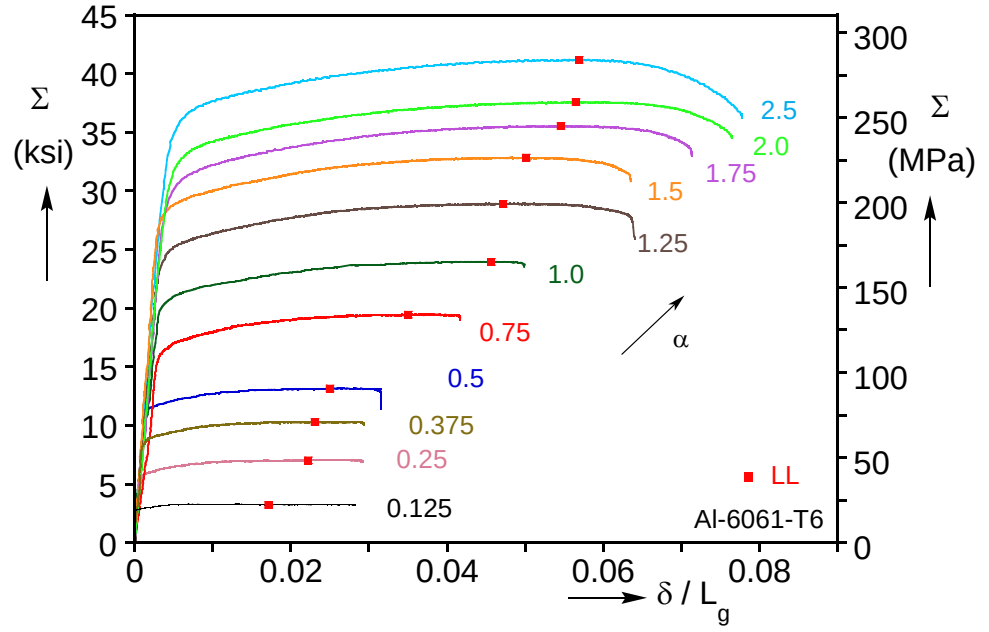

(b)

Figure 3.11: (a) Nominal shear stress-rotation and (b) axial stress-displacement responses for eleven values of α.

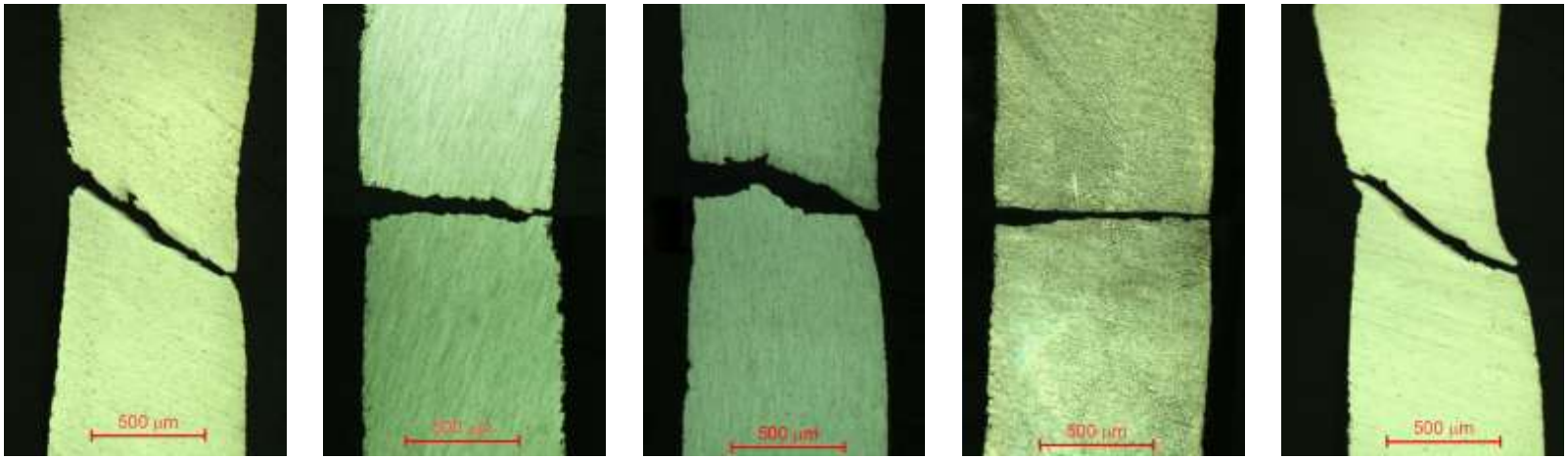

(a) (b) (c) (d) (e)

Figure 3.12: Through thickness sections of specimens showing the mode of failure: (a) $\alpha = 0.25$, (b) $\alpha = 0.75$, (c) $\alpha = 1.0$ $\sigma \rightarrow \tau$, (d) $\alpha = 1.5$, and (e) $\alpha = 2.0$.

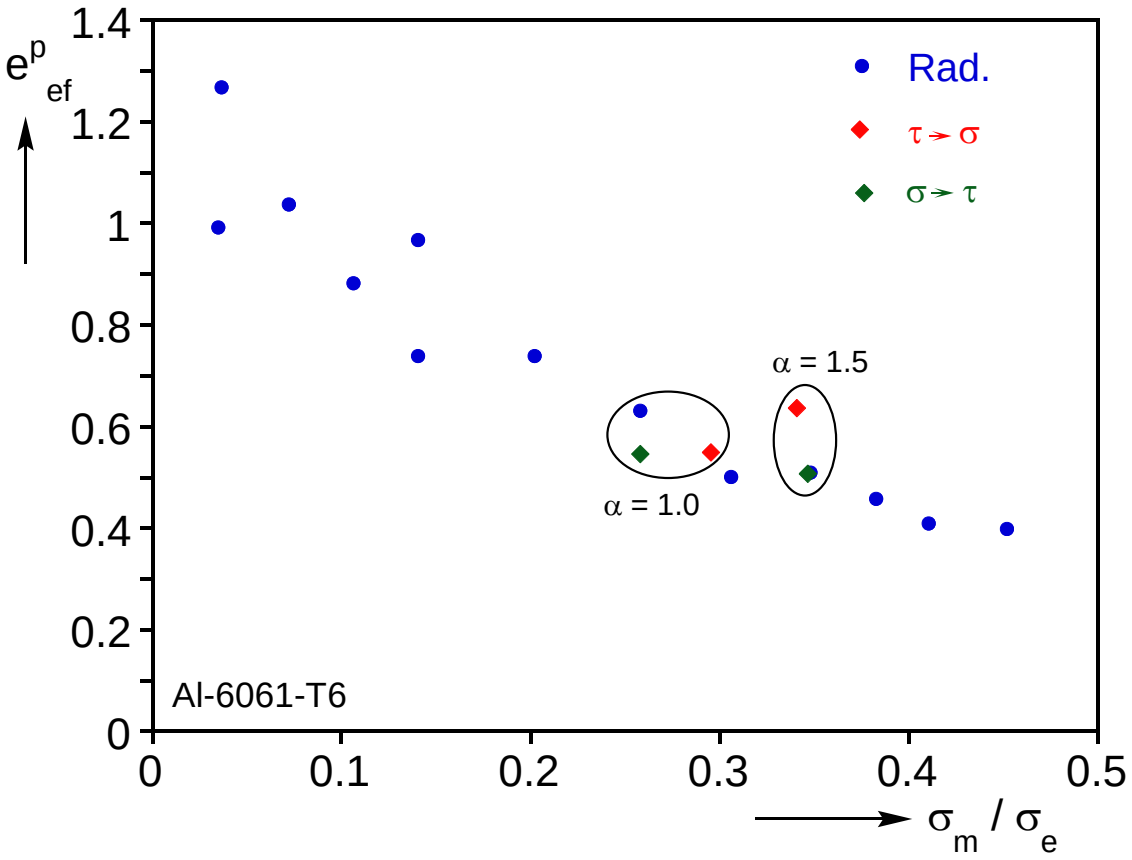

Figure 3.13: Measured equivalent plastic strain at failure as a function of normalized mean stress from 13 radial and 4 corner tension-torsion path experiments.

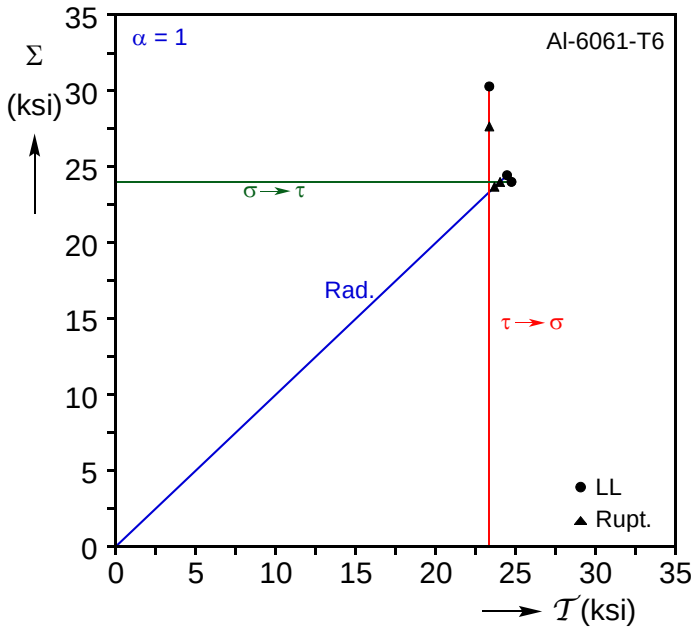

(a)

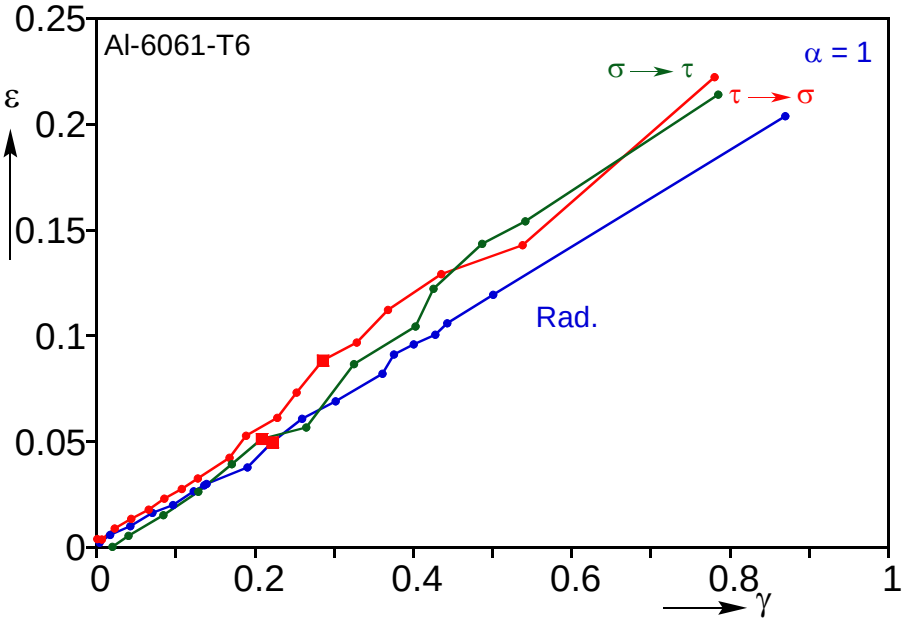

(b)

Figure 3.14: (a) Σ - $\mathcal{T}$ corner stress paths prescribed for $\alpha = 1.0$ including the stress maxima and the values at failure. (b) Induced nominal strain paths.

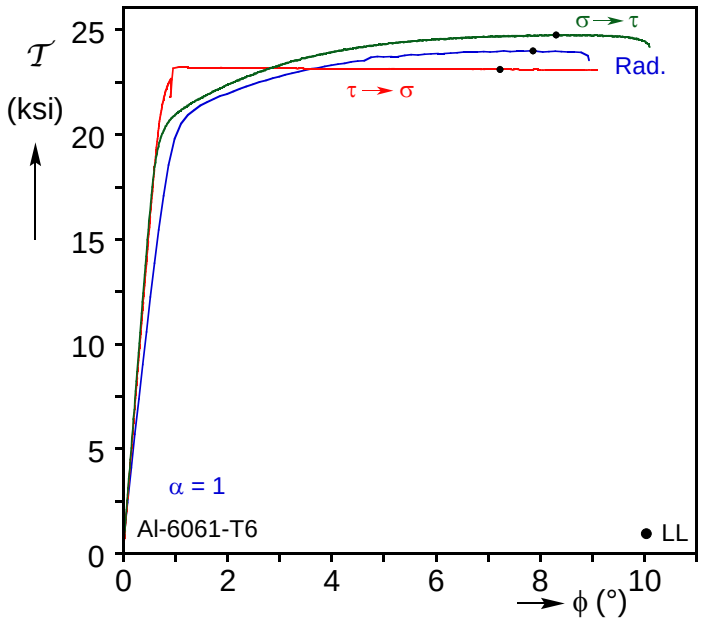

(a)

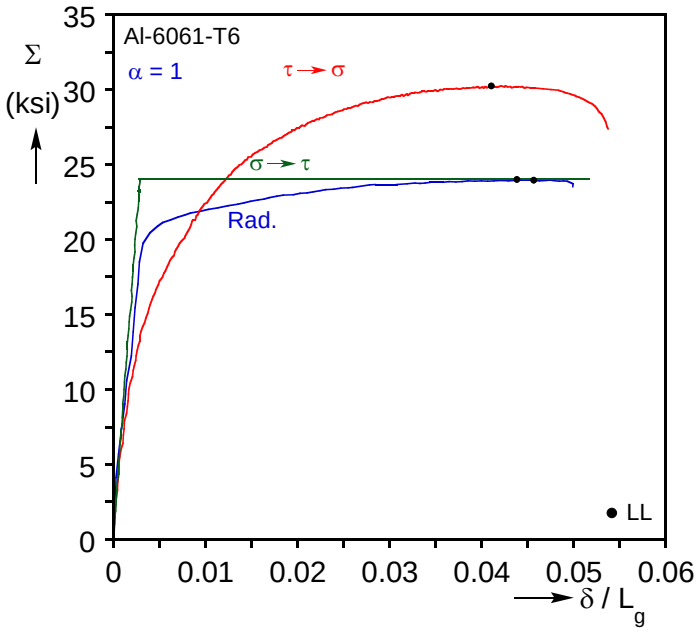

(b)

Figure 3.15: (a) Nominal shear stress-rotation and (b) axial stress-displacement responses for non-radial stress paths for $\alpha = 1.0$.

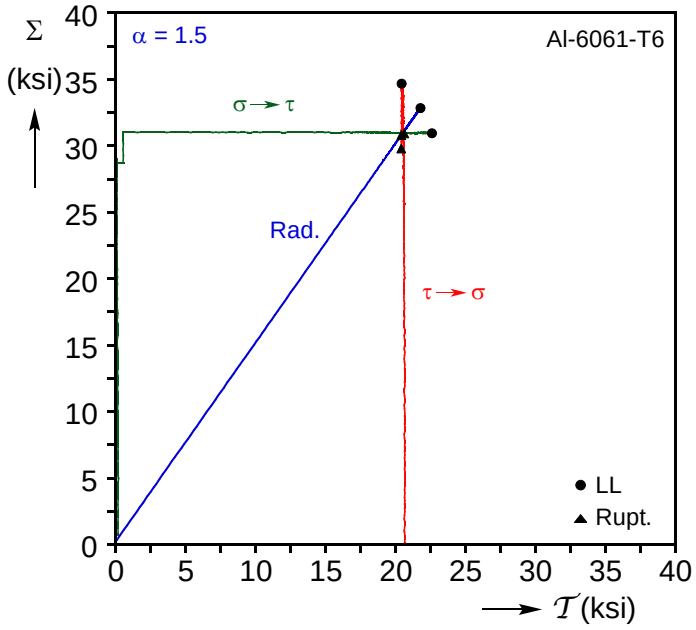

(a)

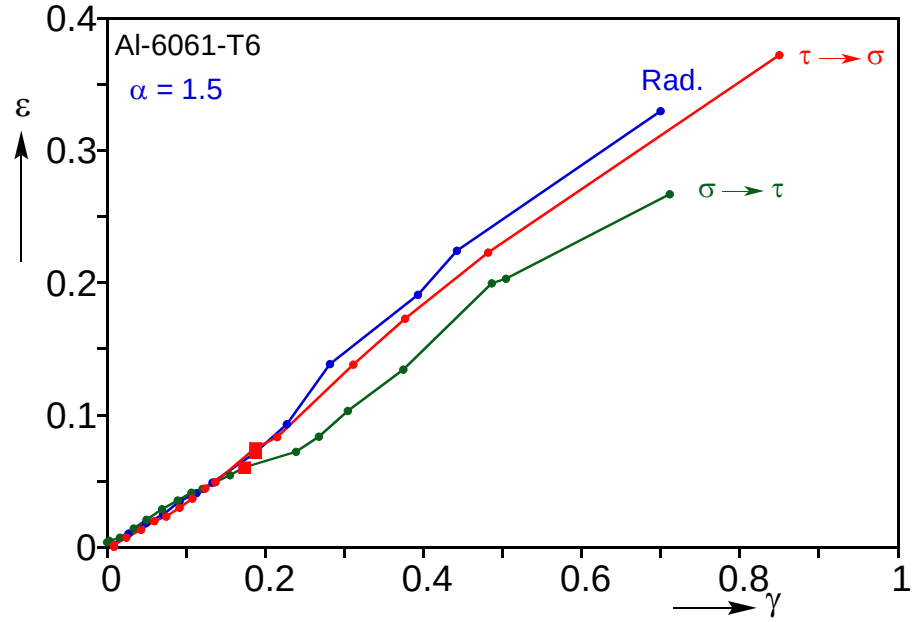

(b)

Figure 3.16: (a) Σ - $\mathcal{T}$ corner stress paths prescribed for $\alpha = 1.5$ including the stress maxima and the values at failure. (b) Induced nominal strain paths.

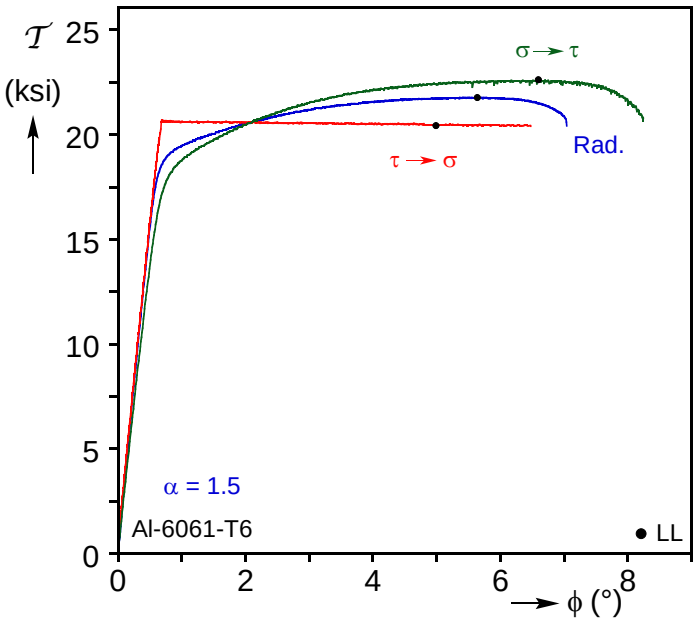

(a)

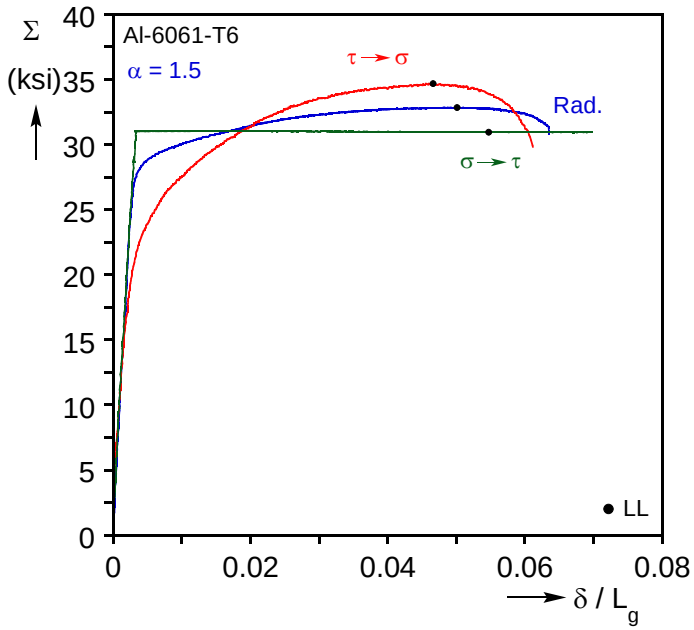

(b)

Figure 3.17: . (a) Nominal shear stress-rotation and (b) axial stress-displacement responses for non-radial stress paths for $\alpha = 1.5$

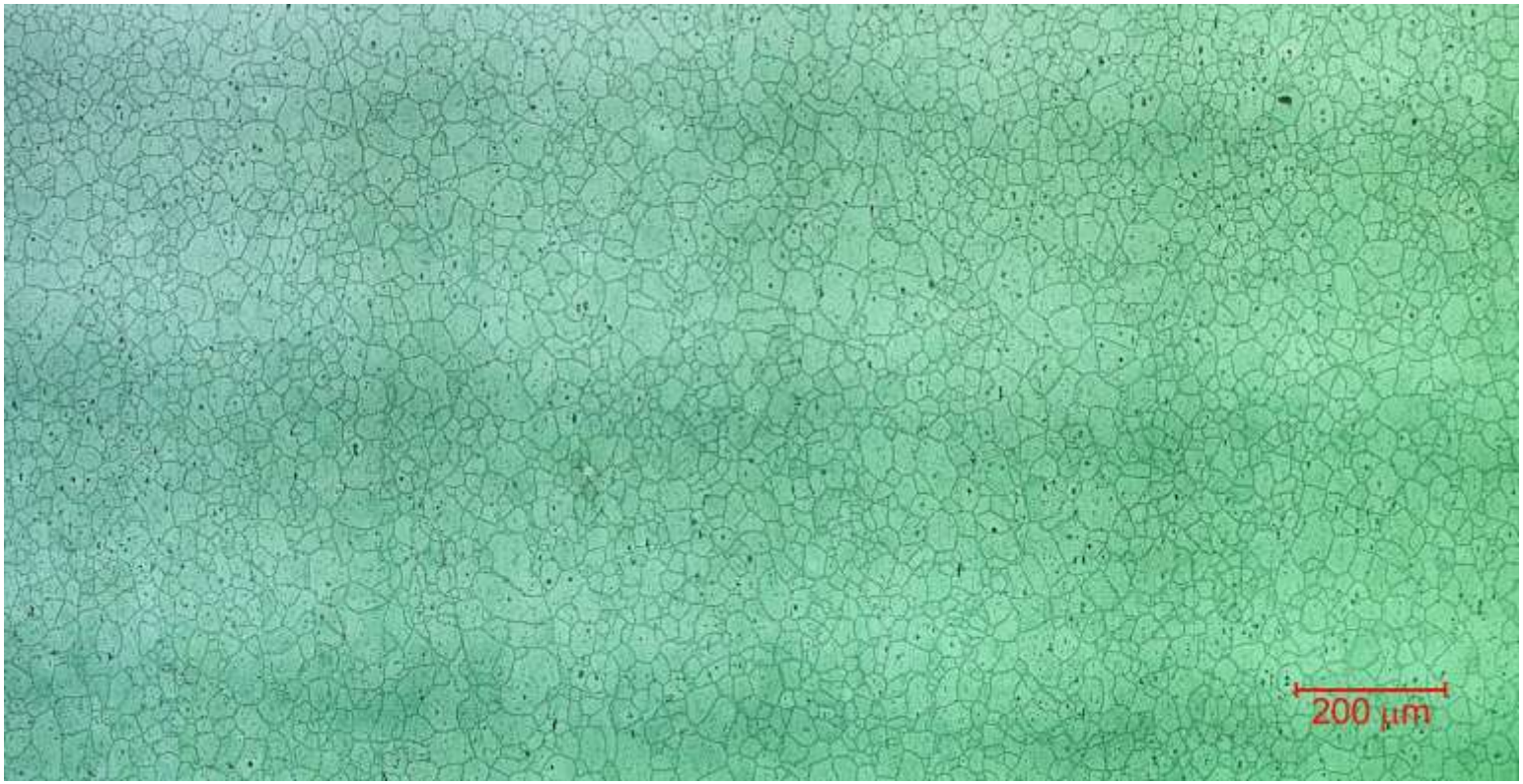

Figure 4.1: Micrograph showing the initial grain microstructure of the Al-6061-T6 tubes used in the tension-torsion experiments (planar view with vertical being along the axis of the tube)- DC13.

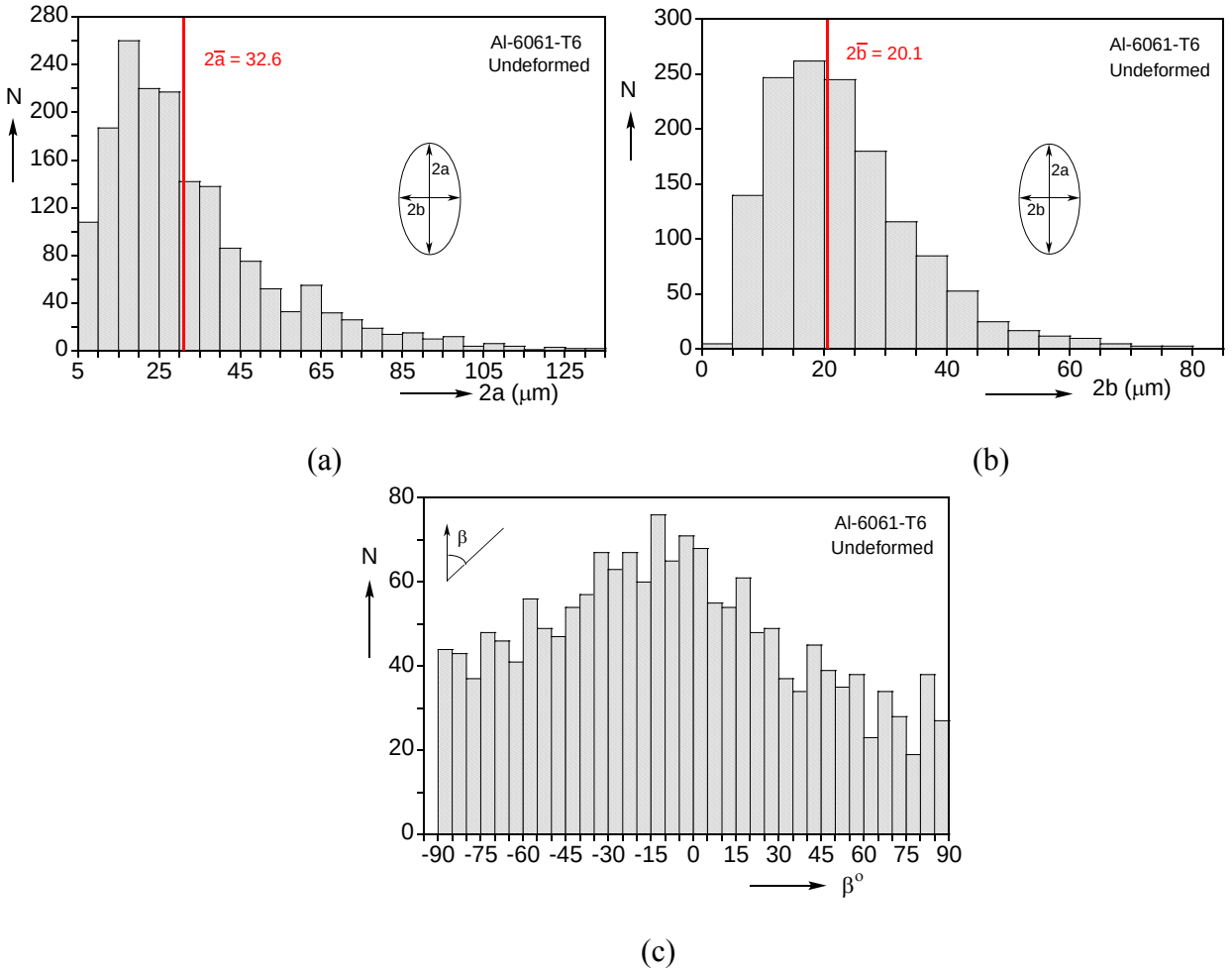

Figure 4.2: In-plane undeformed grain dimension distributions (a) along and (b) transverse to tube axis. (c) Angle between equivalent ellipse major axis and tube axis.

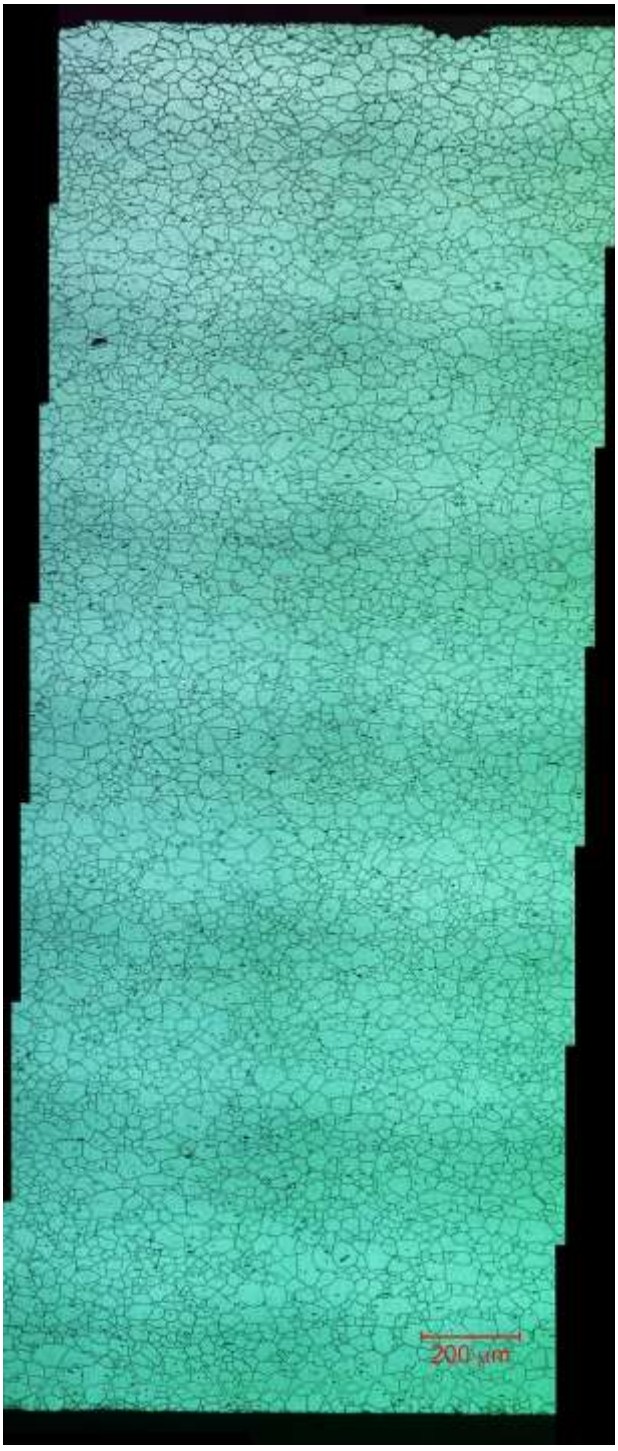

Figure 4.3: Micrograph showing the initial grain microstructure of the Al-6061-T6 tubes used in the tension-torsion experiments (thru thickness view with horizontal being along the axis of the tube)- DC13.

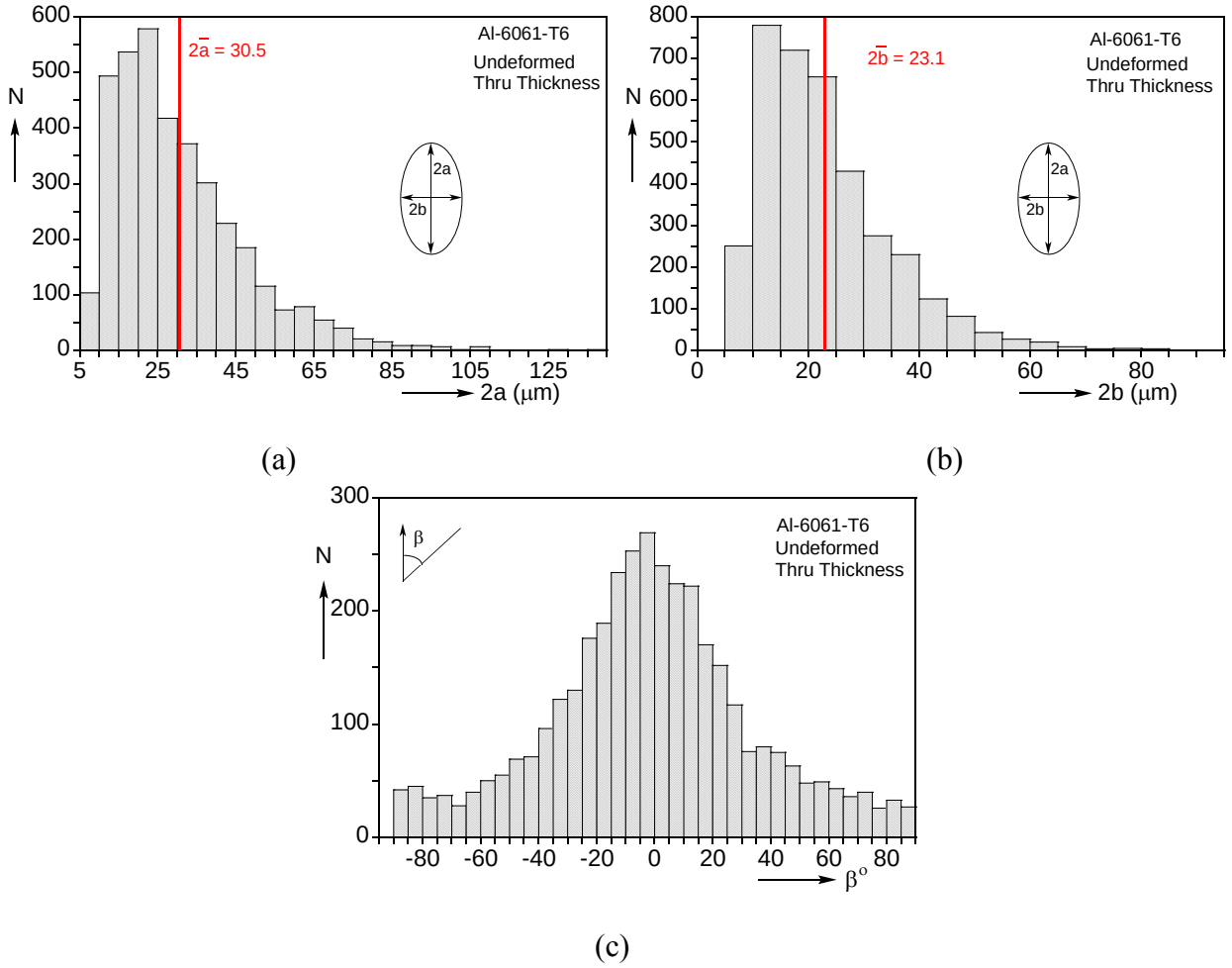

Figure 4.4: Through-thickness undeformed grain dimension distributions (a) along and (b) transverse to tube axis. (c) Angle between equivalent ellipse major axis and tube axis.

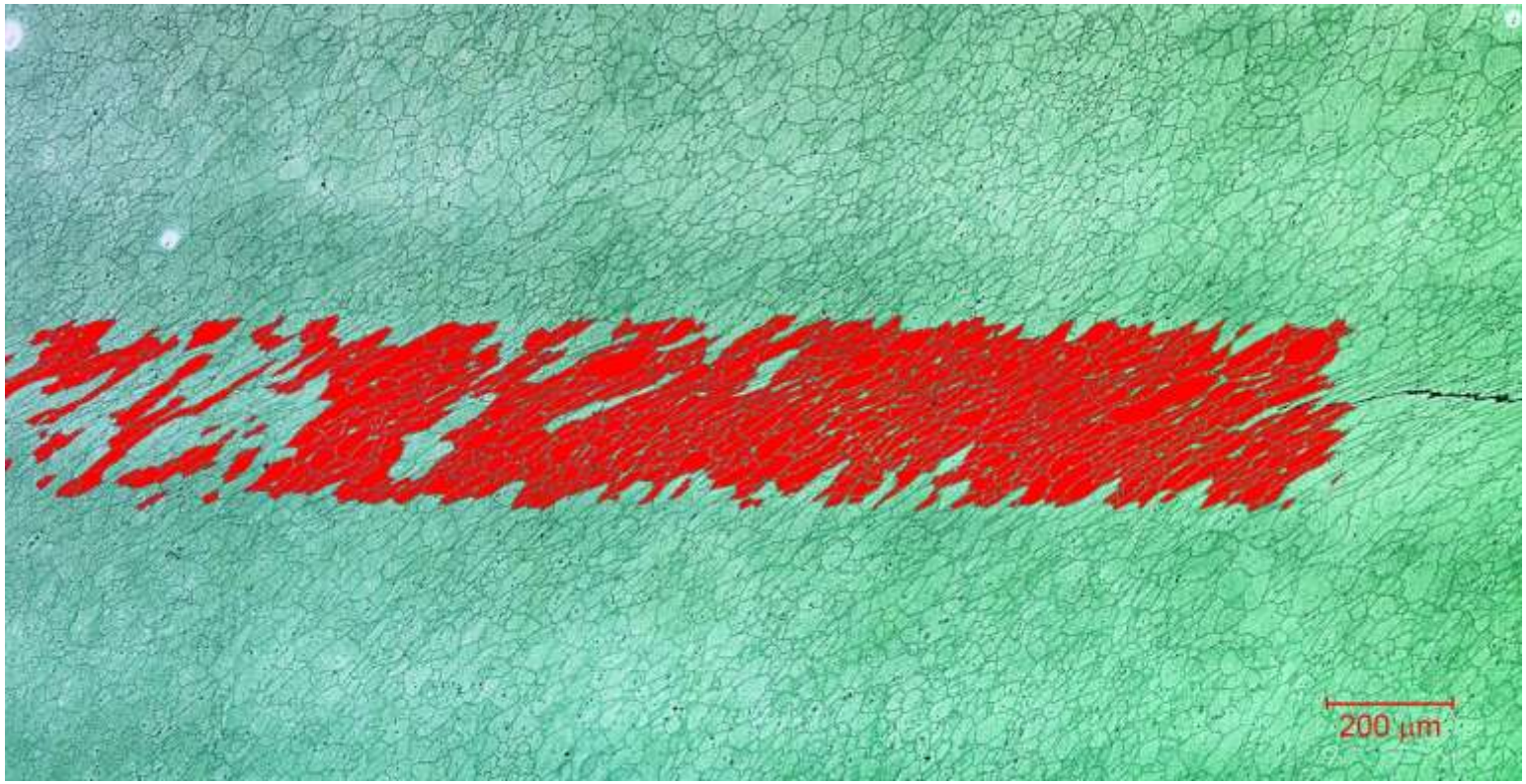

Figure 4.5: Micrograph showing a planar view of the deformed grain microstructure after failure for $\alpha = 0.75$; on the right is the crack (vertical along the axis of the tube). The red grains are used to estimate the grain level deformation- DC13.

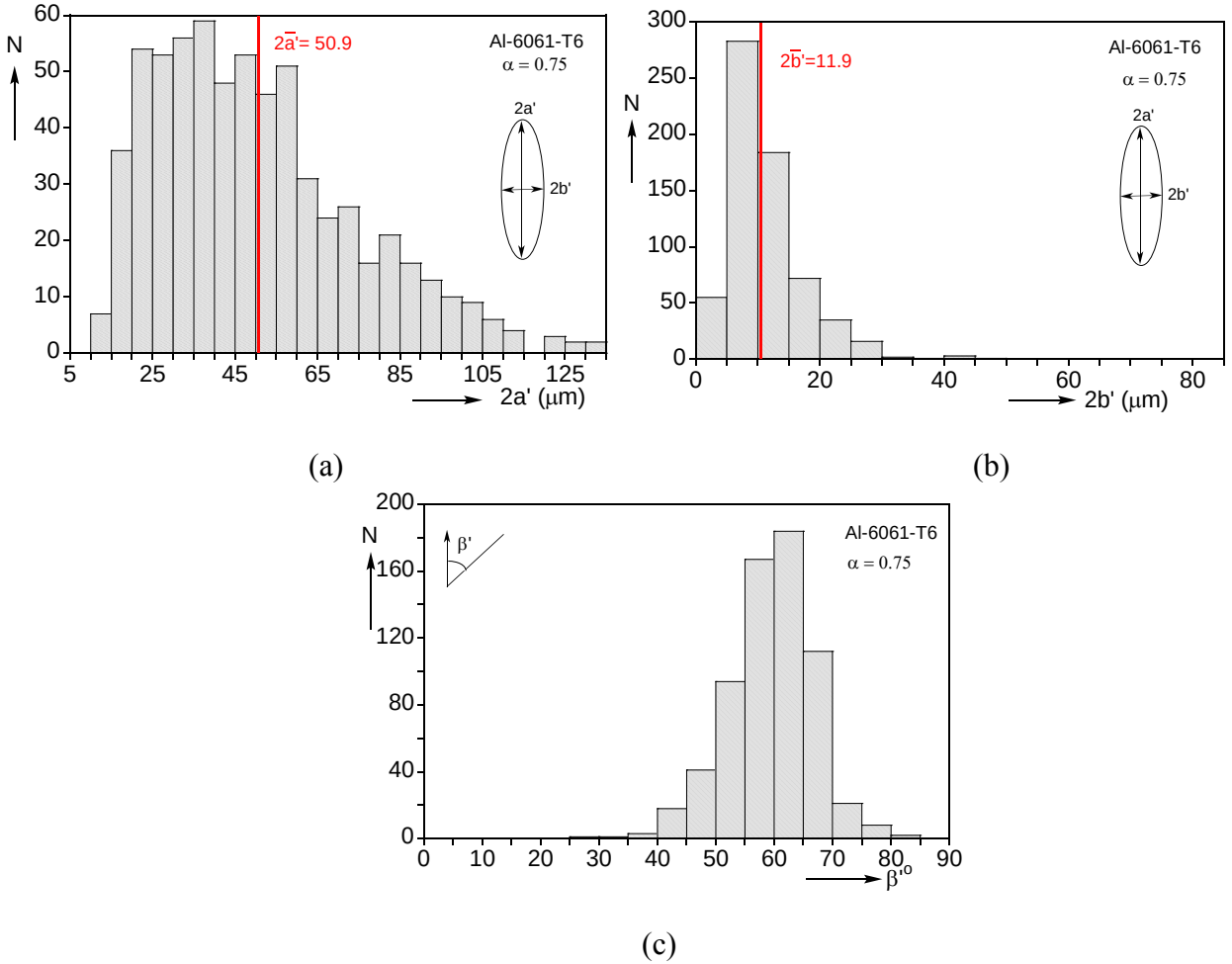

Figure 4.6: In-plane deformed grain dimension distributions (a) major and (b) minor dimensions. (c) Deformed grain angle with tube axis ($\alpha = 0.75$).

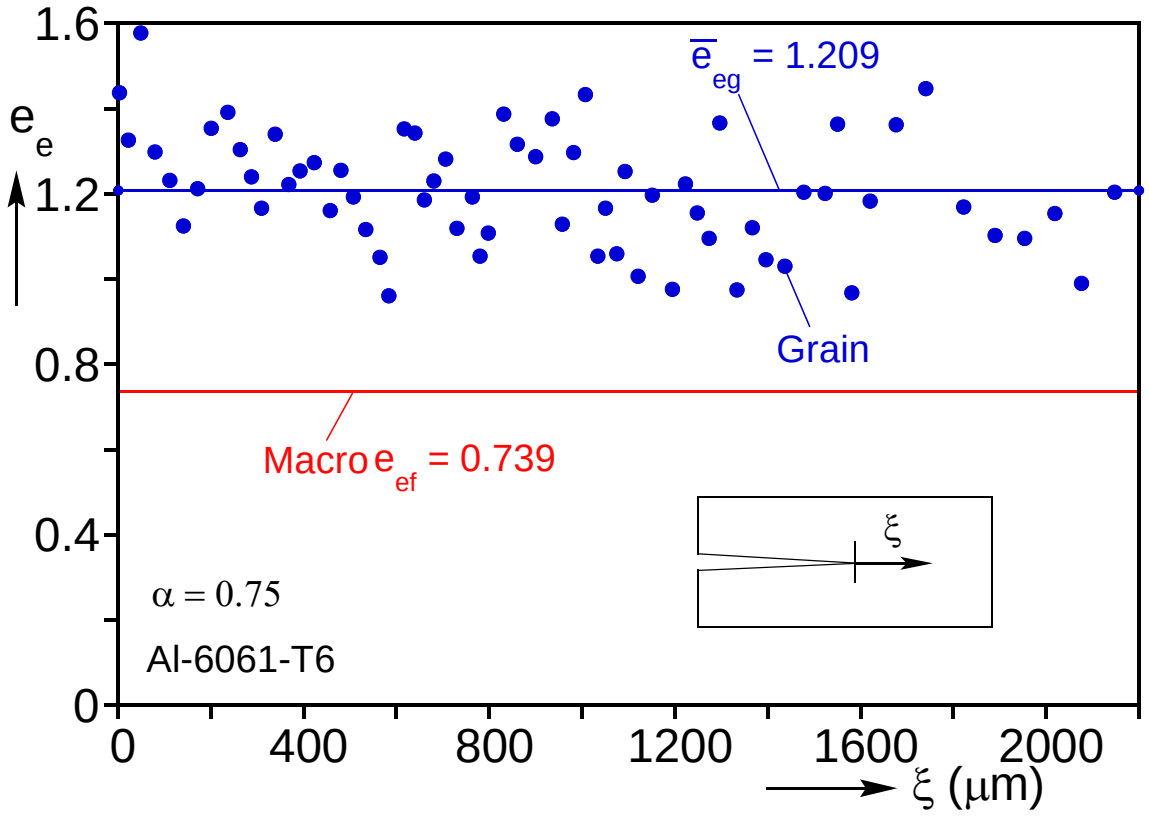

Figure 4.7: Deformed grain strains (average of groups of 10) vs. distance from the crack tip from grains in band shown in Figure 4.5. Included is the strain at failure estimated from the grid—macro ($\alpha = 0.75$).

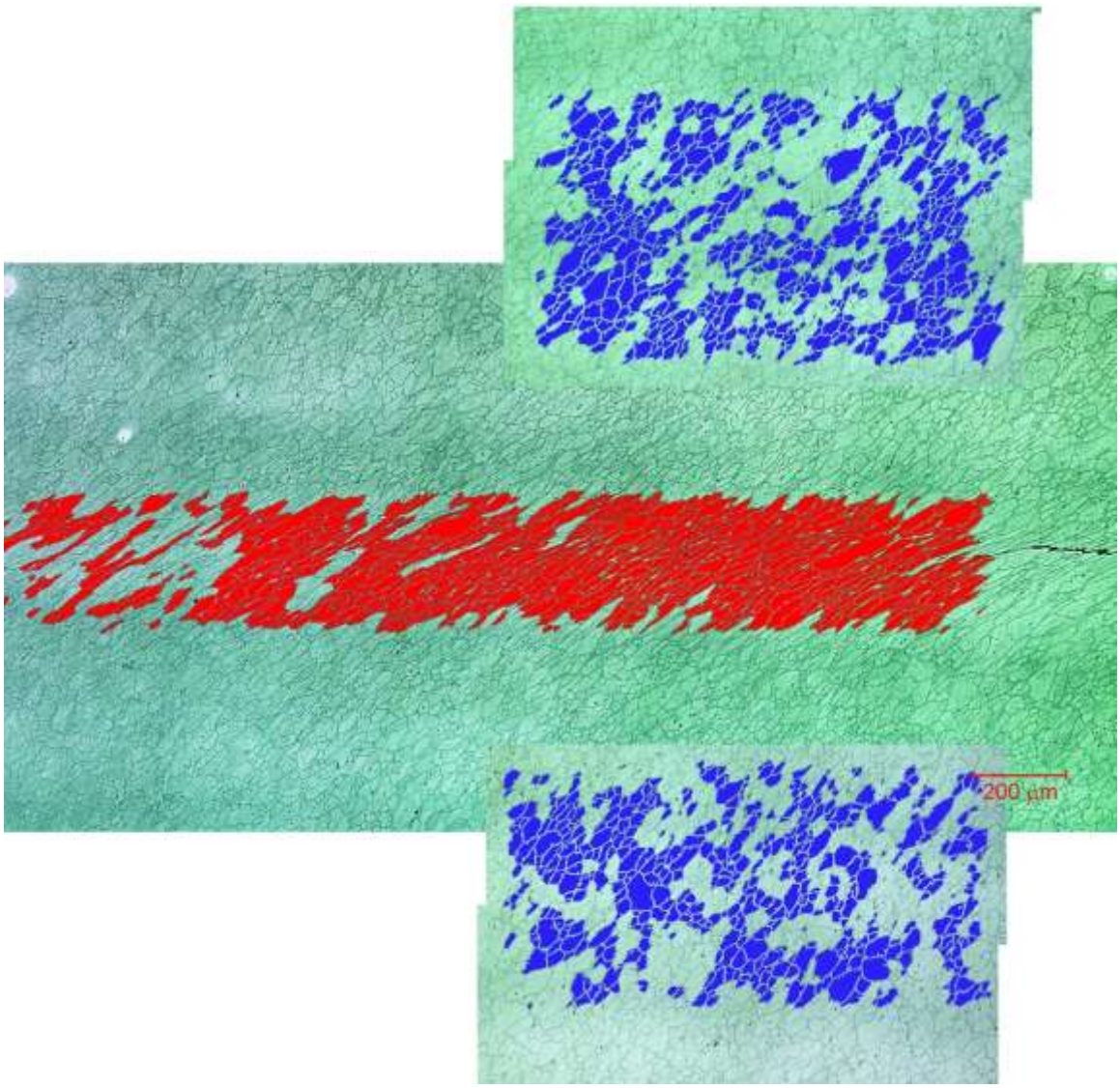

Figure 4.8: Micrograph of deformed grains showing the 300 µm band about the crack and two additional ones on either side of it (α = 0.75).

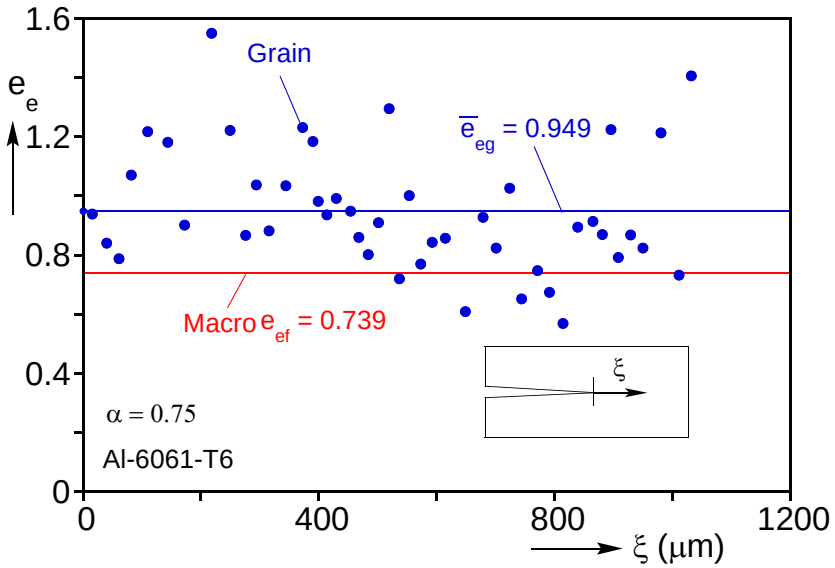

(a)

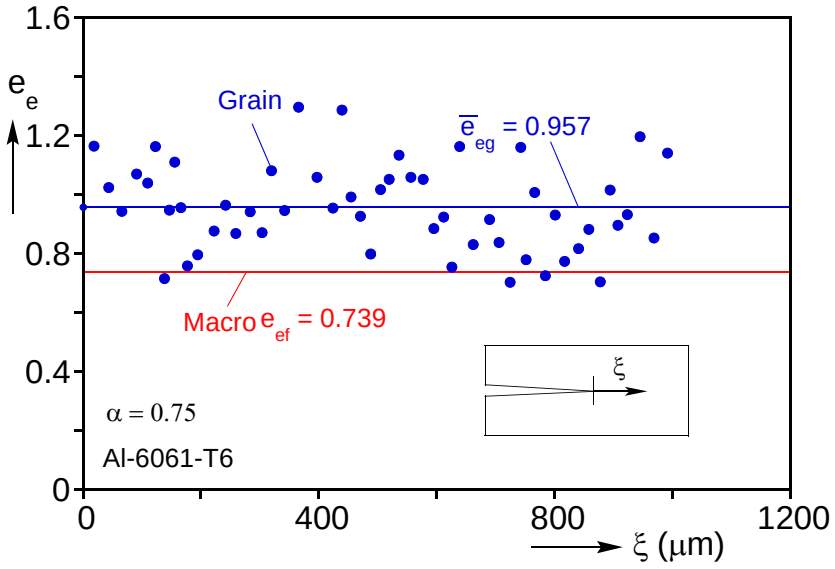

(b)

Figure 4.9: Deformed grain strains (average of groups of 10) vs. distance from the crack tip from grains in bands in Figure 4.8 above and below the crack (α = 0.75).

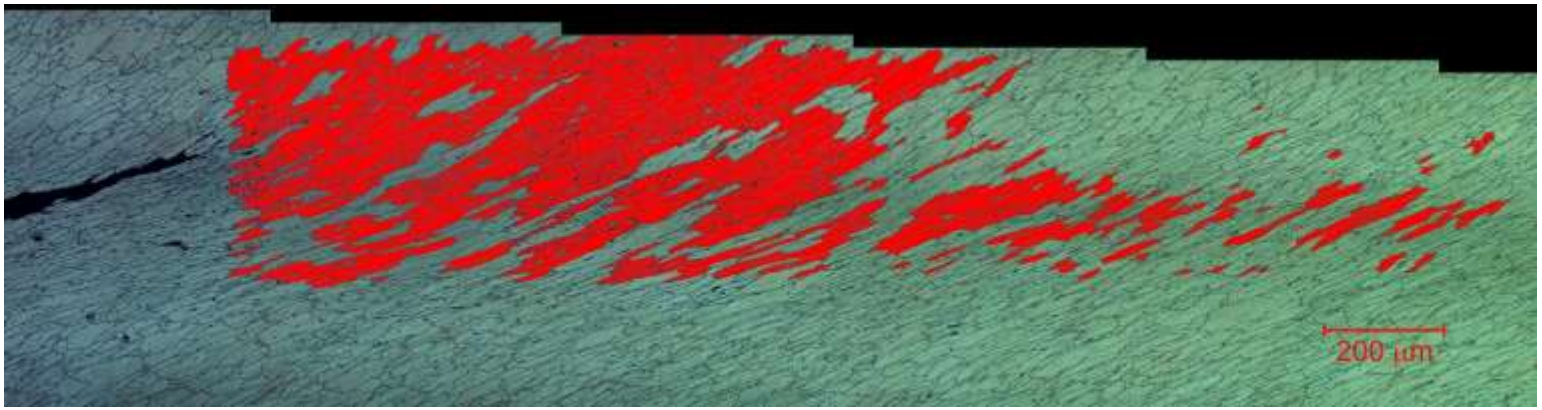

Figure 4.10: Micrograph showing a planar view of the deformed grain microstructure after failure for $\alpha = 0.25$; on the left is the crack (vertical along the axis of the tube). The red grains are used to estimate the grain level deformation- DC13.

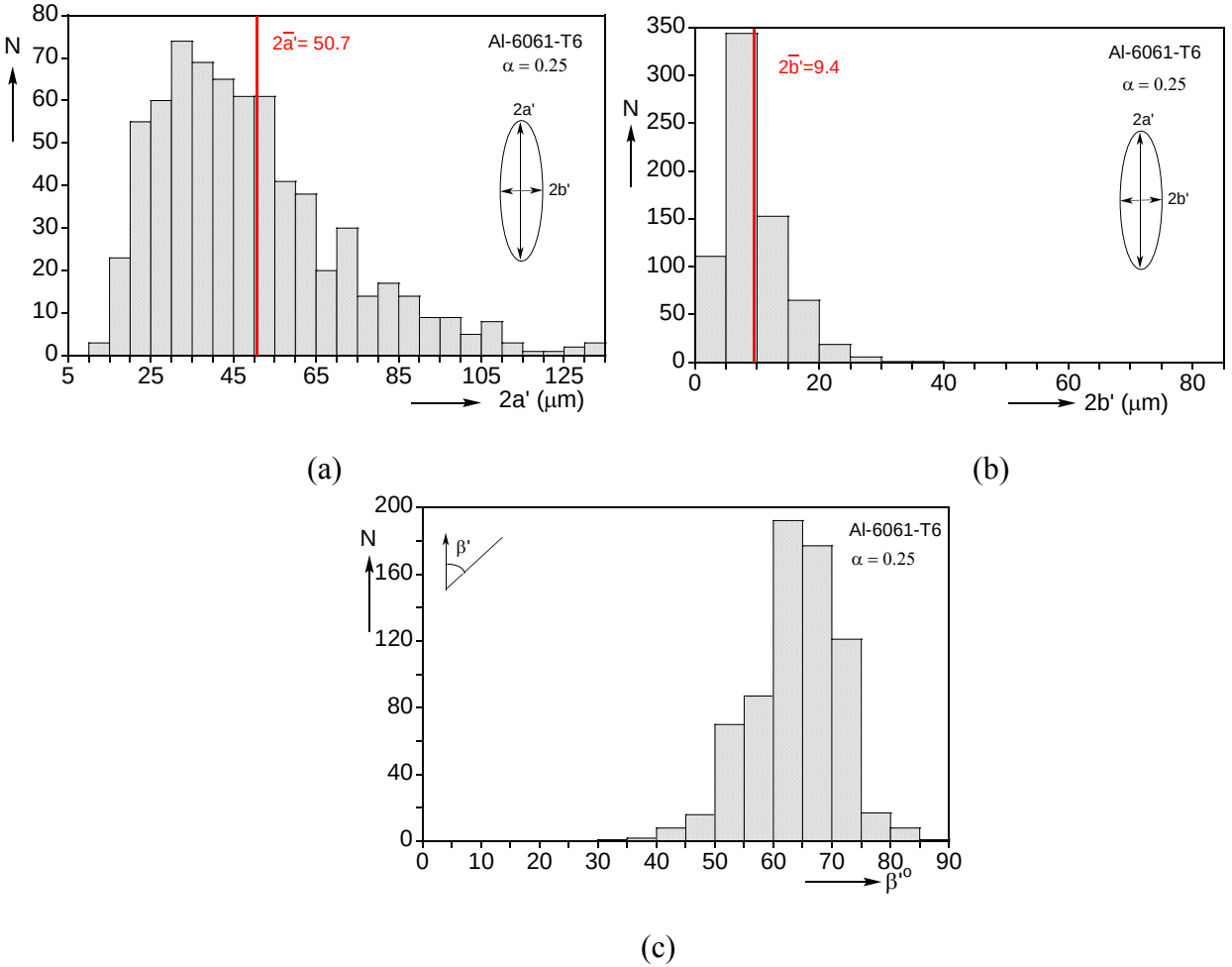

Figure 4.11: In-plane deformed grain dimension distributions (a) major and (b) minor dimensions. (c) Deformed grain angle with tube axis (α = 0.25).

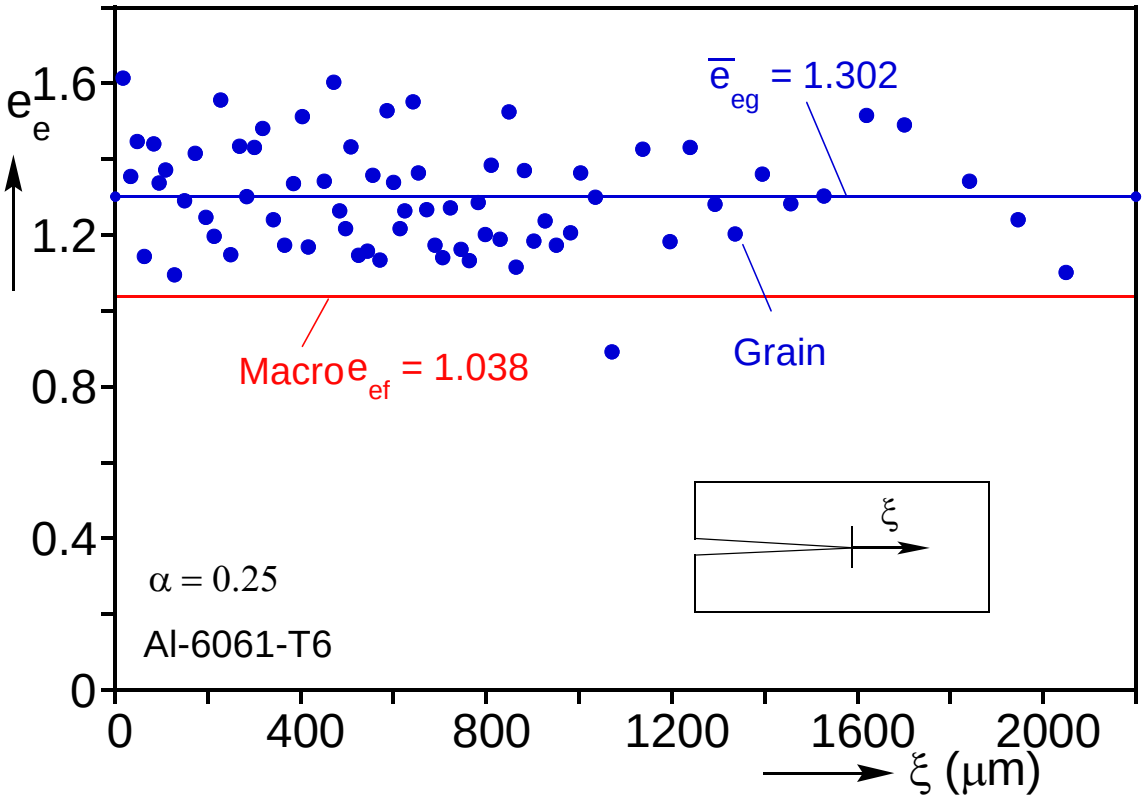

Figure 4.12: Deformed grain strains (average of groups of 10) vs. distance from the crack tip from grains in band shown in Figure 4.10. Included is the strain at failure estimated from the grid—macro (α = 0.25).

Figure 4.13: Micrograph showing a planar view of the deformed grain microstructure after failure for α = 1.0 $\sigma \rightarrow \tau$; on the left is the crack (vertical along the axis of the tube). The red grains are used to estimate the grain level deformation- DC13.

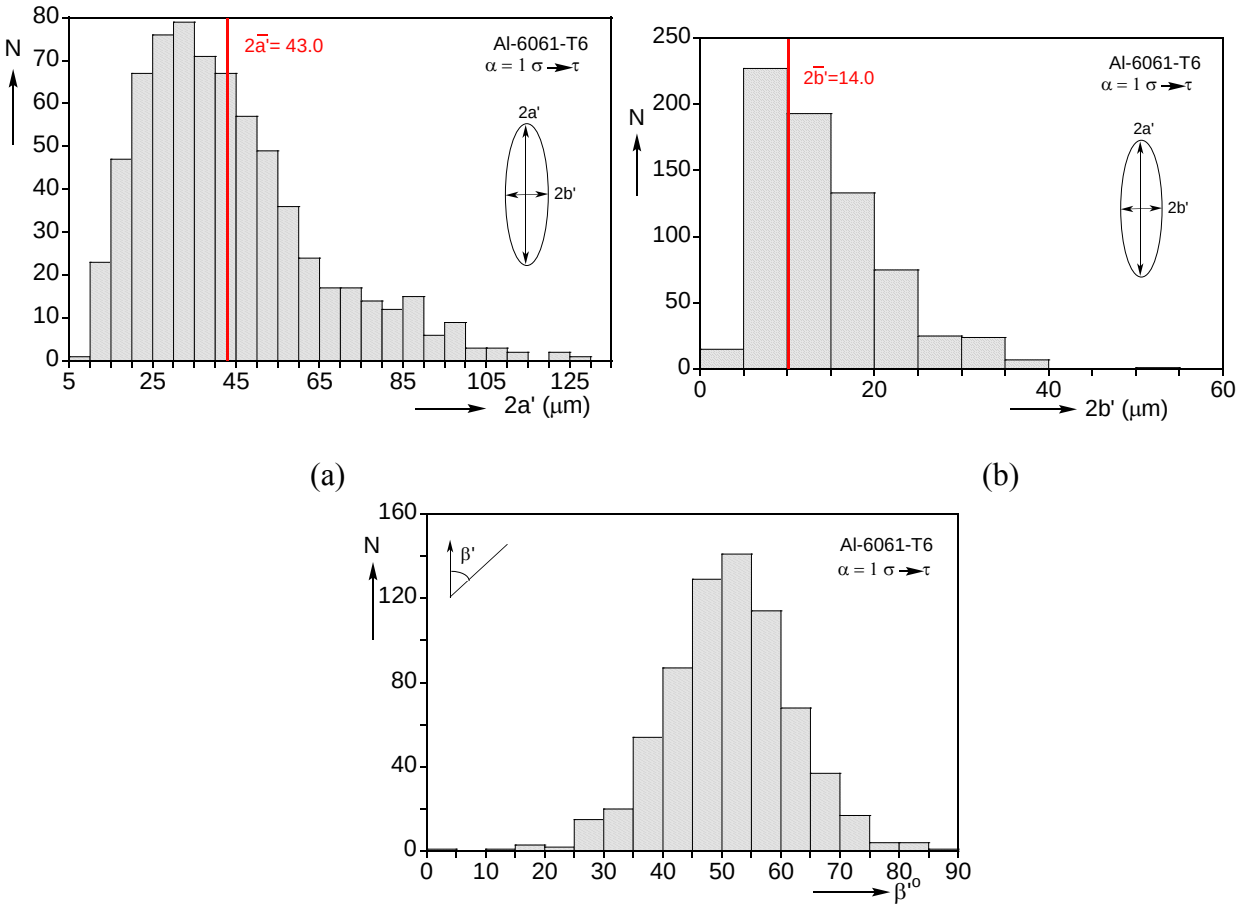

Figure 4.14: In-plane deformed grain dimension distributions (a) major and (b) minor dimensions. (c) Deformed grain angle with tube axis (α = 1.0 σ→ τ).

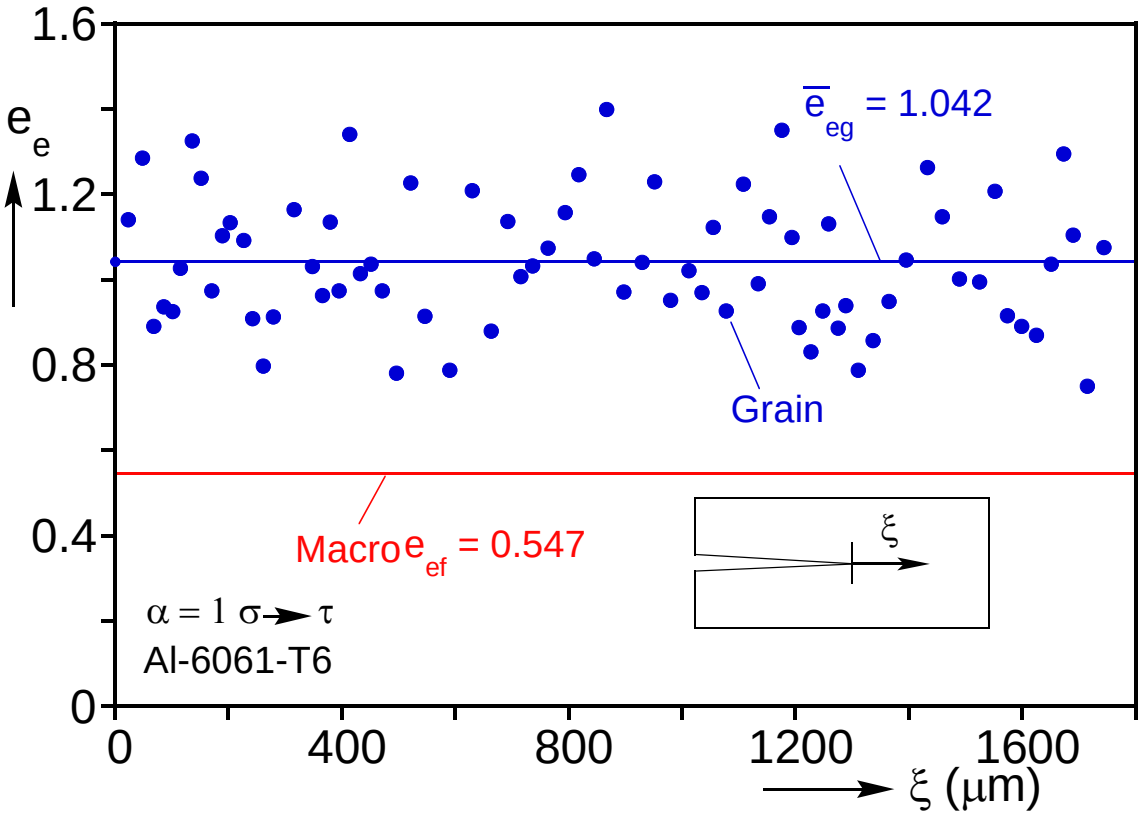

Figure 4.15: Deformed grain strains (average of groups of 10) vs. distance from the crack tip from grains in band shown in Figure 4.13. Included is the strain at failure estimated from the grid—macro (α = 1.0 σ→ τ).

Figure 4.16: Micrograph showing a planar view of the deformed grain microstructure after failure for α = 1.5; on the left is the crack (vertical along the axis of the tube). The red grains are used to estimate the grain level deformation- DC13.

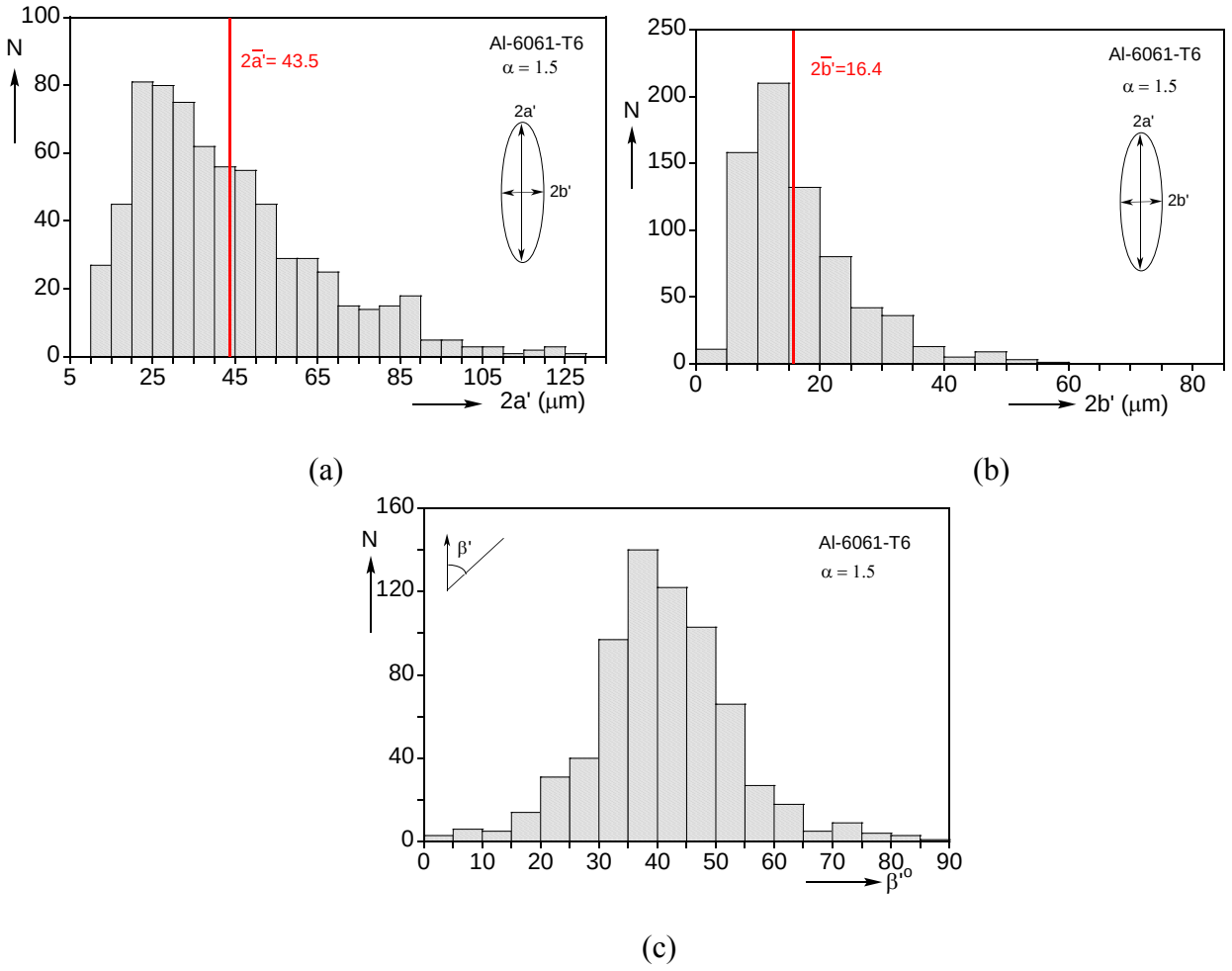

Figure 4.17: In-plane deformed grain dimension distributions (a) major and (b) minor dimensions. (c) Deformed grain angle with tube axis (α = 1.5).

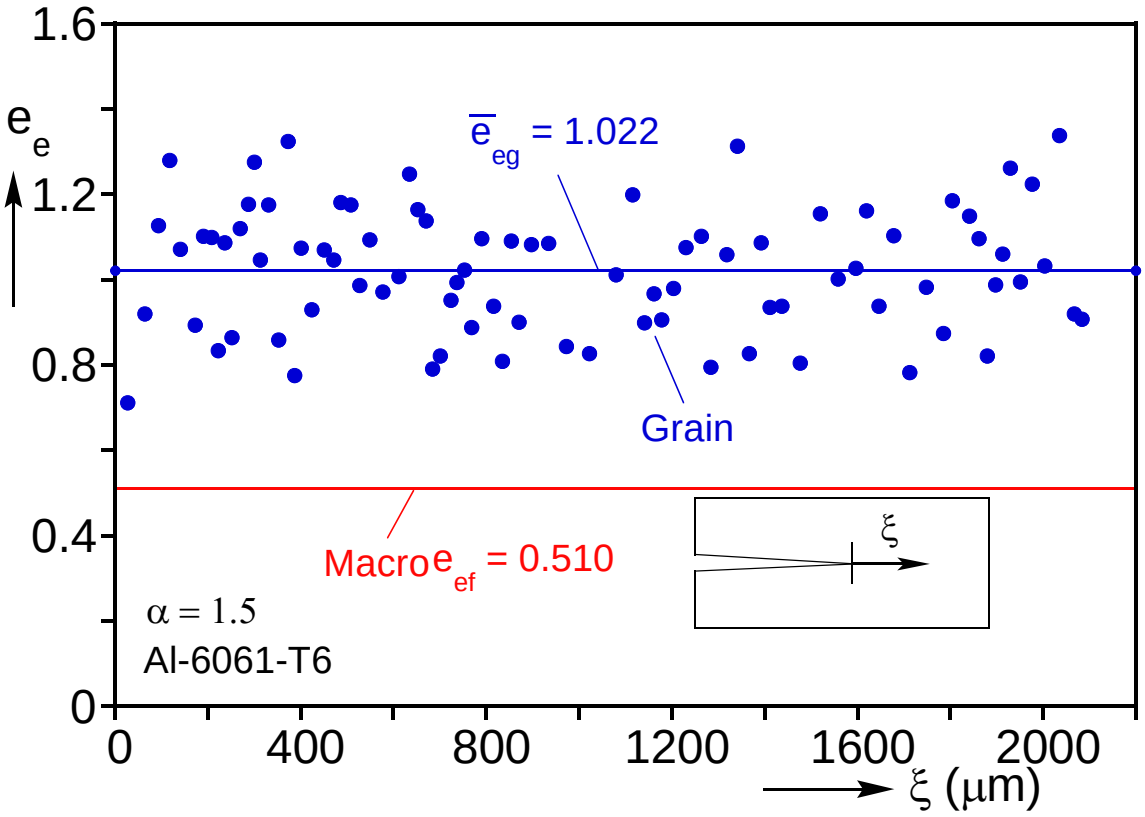

Figure 4.18: Deformed grain strains (average of groups of 10) vs. distance from the crack tip from grains in band shown in Figure 4.16. Included is the strain at failure estimated from the grid—macro (α = 1.5).

Figure 4.19: Micrograph showing a planar view of the deformed grain microstructure after failure for $\alpha = 2.0$; on the left is the crack (vertical along the axis of the tube). The red grains are used to estimate the grain level deformation- DC13.

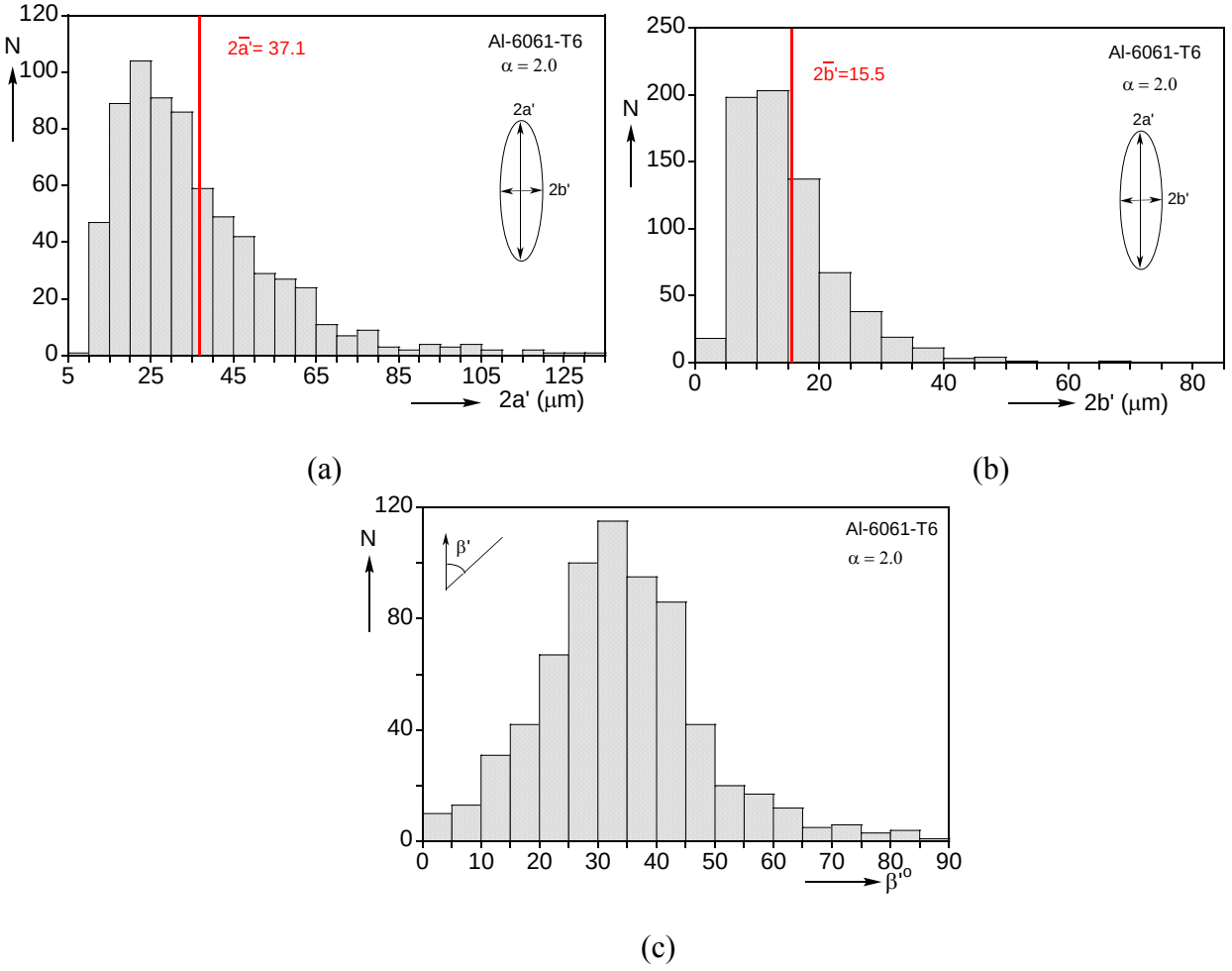

Figure 4.20: In-plane deformed grain dimension distributions (a) major and (b) minor dimensions. (c) Deformed grain angle with tube axis (α = 2.0).

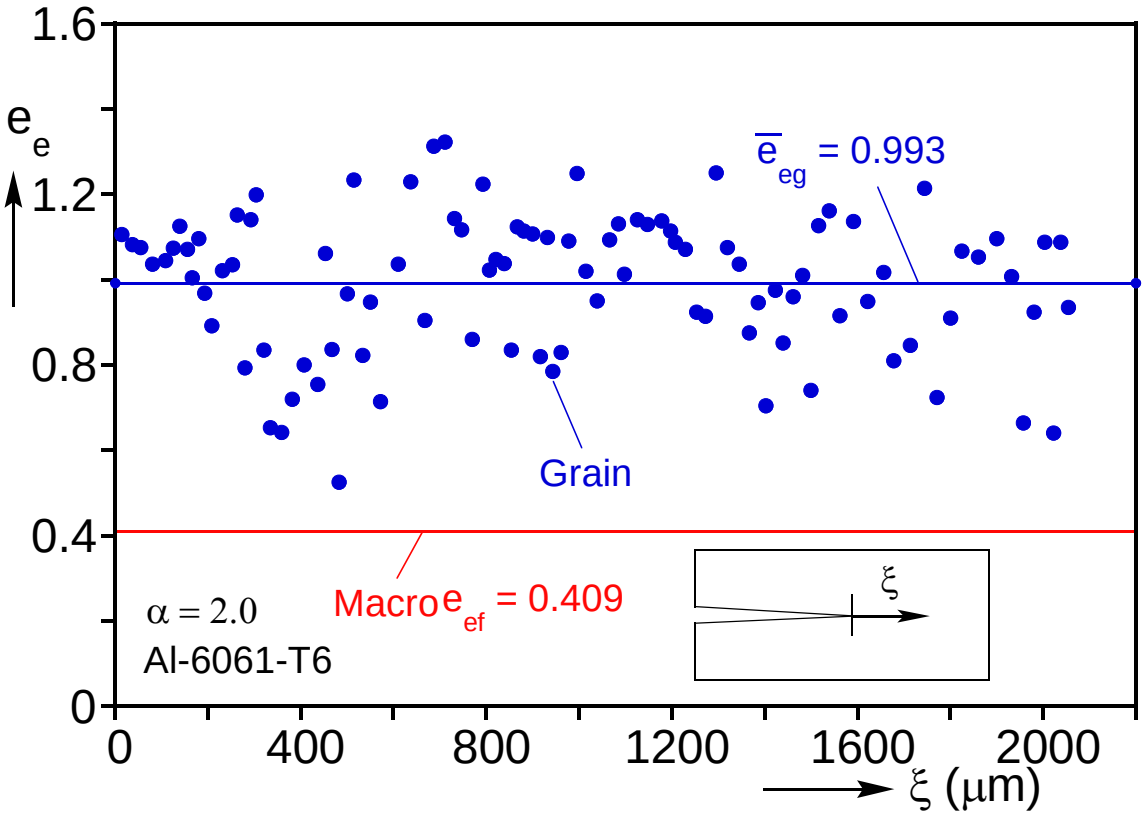

Figure 4.21: Deformed grain strains (average of groups of 10) vs. distance from the crack tip from grains in band shown in Figure 4.19. Included is the strain at failure estimated from the grid—macro (α = 2.0).

Appendix: Extraction of Stress Strain Responses

Using the data recorded during the experiments, stress-strain curves were generated in order to allow for future constitutive modeling including calibration of anisotropies. The strains calculated from the time lapse photographs can be synchronized with the axial and shear stresses calculated from the axial and torsional load cells. These strains are reliable for large values; however, small strain measurements are subject to the limitations imposed by the pixel size of the images taken. A new technique was therefore needed to generate strain values in the elastic and early plastic regimes. A two-step process of scaling the measurements was utilized to generate strains in these regions using the displacements recorded by the laser extensometer and the rotations recorded by the rotation transducer integral to the machine.

The first step required scaling the displacements and rotations such that the results were forced to produce the expected elastic and shear moduli. For the laser extensometer measurements, this meant choosing a "gage length" to divide the displacement measurements by. This gage length was consistently found to be around 0.6 inches (15.24 mm), which corresponds roughly to the overall width of the groove in the tubular specimen (see Figure 2.1a).

Similarly, the rotation was converted to a shear strain that would match the shear modulus. Since the rotation measurements also included the compliance of the grips and thick section of the tube, a new "gage rotation" was calculated by subtracting the amount the thick part of the exposed tube was expected to rotate based on the simple elastic equation below

$$\varphi = \frac{TL}{GI_P} \tag{A1}$$

where φ is the rotation of the un-gripped, thick section of the tube, T is the torque measured during the experiment, L is the length of the un-gripped, thick section, G is the

shear modulus, and I_P is the second polar moment of area of the cross section of the thick part of the tube. Next, the "gage rotation" was calculated by subtraction as follows.

$$\varphi_G = \varphi_{total} - \varphi \tag{A2}$$

Then, a characteristic gage length was chosen such that the shear strain calculated using the following equation would fit the shear modulus of the aluminum.

$$\gamma = \tan^{-1}\left(\frac{\varphi_G R_m}{L_{\gamma G}}\right) \tag{A3}$$

where R_m is the mid-surface radius of the test section and $L_{\gamma G}$ is the characteristic gage length. These variables can also be seen in Figure A.1. These results were used in the elastic regime and early on in the plastic regime (shear strain <1%).

The second step in the process involved utilizing the same equations and techniques from fitting the elastic section with slightly different gage lengths to bridge the values from the first step to the large strain values extracted from the time lapse photography. The gage lengths for the second step were generally around 0.65 in (16.5 mm), so they were not substantially different from the elastic gage lengths.

Finally, the two steps were connected and linked to the results from the grid analysis. This procedure was executed for experiments with α values of 0.5, 1.0, 1.5, 2.0, and 2.5.The axial and shear stress-strain responses are plotted in Figure A.2.

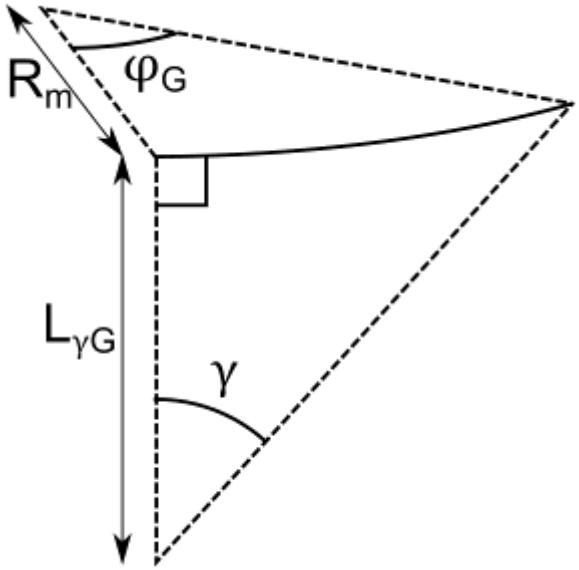

Figure A.1: Geometry of test section used to calculate shear strains at small values.

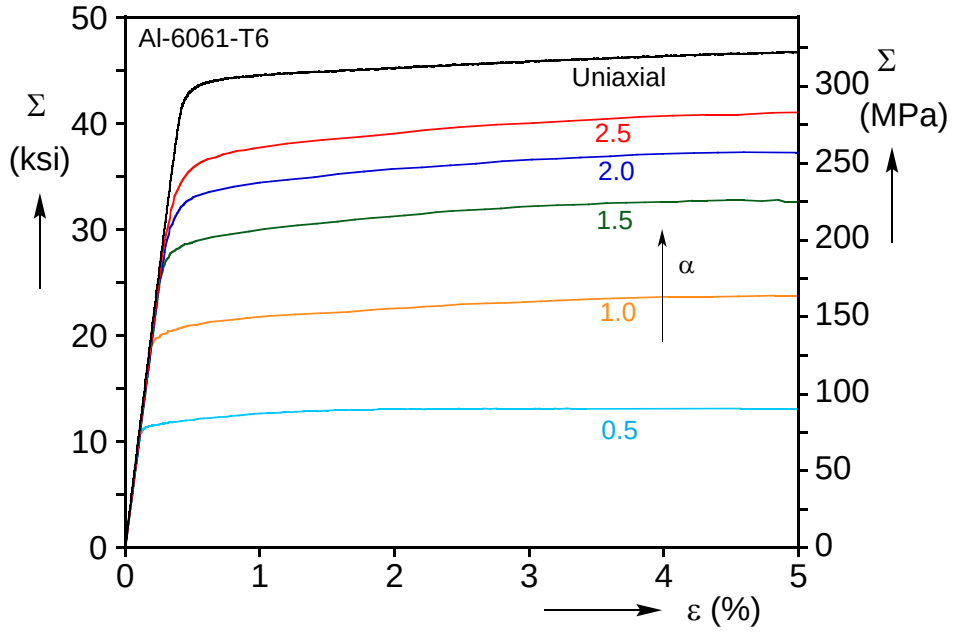

(a)

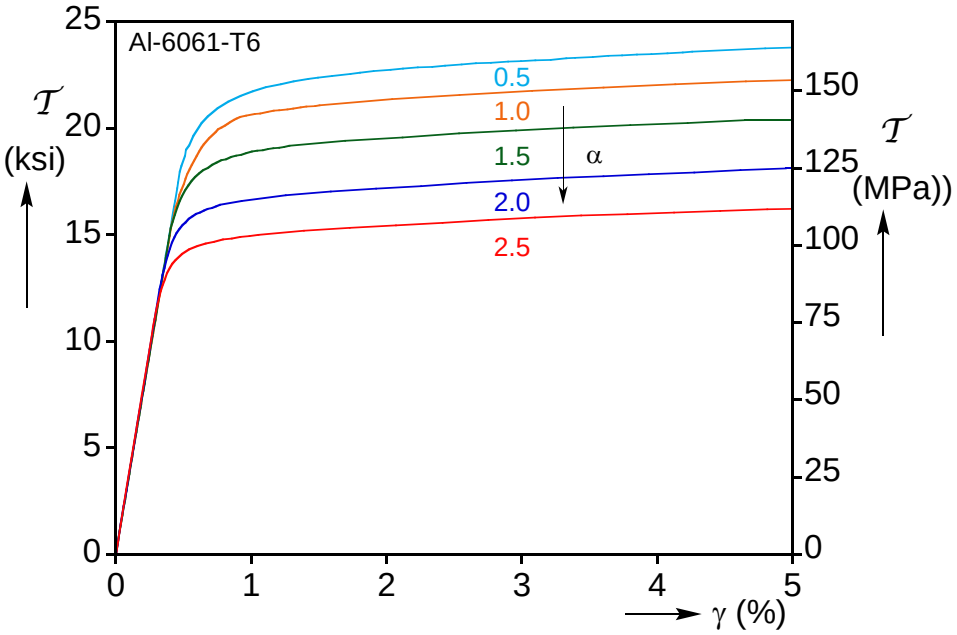

(b)

Figure A.2: (a) Extracted axial stress-strain responses for several different radial loading paths (included is the measured uniaxial tension response) and (b) corresponding shear stress-strain response.

References

Bao, Y.-B. and Wierzbicki, T. (2004). On fracture locus in the equivalent strain and stress triaxiality space. *Int'l J. Mech. Science* **46**, 81-98.

Bai, Y.-L. and Wierzbicki, T. (2008). A new model of metal plasticity and fracture with pressure and Lode dependence. *Int'l J. Plasticity* **24**, 1071-1096

Bai, Y.-L. and Wierzbicki, T. (2010). Application of extended Mohr-Coulomb criterion to ductile fracture. *Int'l J. Fracture* **161**, 1-20

Barsoum, I. and Faleskog, J., 2007. Rupture mechanisms in combined tension and shear– Experiments. *Int'l J. Solids Struct.* **44**, 1768-1786.

Beese, A.,M., Luo, M., Li, Y., Bai, Y., Wierzbicki, T., 2010. Partially coupled anisotropic fracture model for aluminum sheets. *Eng. Fract. Mech.* **77**, 1128-1152.

Davis, J. R. Metallographic Technique for Nonferrous Metals and Special-Purpose Alloys. Ed. G. F. Vander Voort. *Metals Handbook.* Materials Park, OH: ASM International, 1998.1356-1409. Print.

Dunand, M., Mohr, D., 2010. Hybrid experimental-numerical analysis of basic ductile fracture experiments for sheet metals. *Int'l J. Solids Struct.* **47**, 1130-1143.

Dunand, M., Mohr, D., 2011. Optimized butterfly specimen for the fracture testing of sheet materials under combined normal and shear loading. *Eng. Fract. Mech.* **78**, 1128-1152.

Ghahremaninezhad, A. and Ravi-Chandar, K., 2011. Ductile failure in polycrystalline OFHC copper. *Int'l J. Solids Struct.* **48**, 3299-3311.

Ghahremaninezhad, A. and Ravi-Chandar, K., 2012. Ductile failure in polycrystalline Al 6061-T6. *Int'l J. Fracture* **174**, 177-202

Giagmouris, T., Kyriakides, S., Korkolis, Y.P., and Lee, L.-H., 2010. On the localization and failure in aluminum shells due to crushing induced bending and tension. *Int'l J. Solids Struct.* **47**, 2680-2692.

Haltom, S. S., Kyriakides, S.K., Ravi-Chandar, K. (2012) "Ductile failure under combined shear and tension." *International Journal of Solids and Structures*. (Submitted August 2012)

Johnson, G.R. and Cook, W.H., 1985. Fracture characteristics of three metals subjected to various strains, strain rates, temperatures and pressures. *Eng. Fracture Mech.* **21**, 31-48.

Khan, A.S. and Liu, H., 2012. A new approach for ductile fracture prediction on Al-2024-T351 alloy. *Int'l J. Plasticity* **35**, 1-12.

Korkolis, Y.P. and Kyriakides, S., 2008a. Inflation and burst of anisotropic aluminum tubes for hydroforming applications. *Int'l J. Plasticity* **24**, 509-543.

Korkolis, Y.P. and Kyriakides, S., 2008b. Inflation and burst of anisotropic aluminum tubes Part II: An advanced yield function including deformation-induced anisotropy. *Int'l J. Plasticity* **24**, 1625-1637.

Korkolis, Y.P. and Kyriakides, S., 2009. Path-dependent failure of inflated aluminum tubes. *Int'l J. Plasticity* **25**, 2059-2080.

Korkolis, Y.P., Kyriakides, S., Giagmouris, T., Lee, L.-H., 2010. Constitutive modeling and rupture predictions of Al-6061-T6 tubes under biaxial loading paths. *ASME J. Applied Mechanics* **77**:5, 064501, 1-5.

McClintock, F.A., 1968. A criterion for ductile fracture by growth of holes. *ASME J. Applied Mech.* **35**, 363-371.

McClintock, F.A., 1971. Plasticity Aspects of Fracture. In, *Fracture an Advanced Treatise* Vol. III, Ed. Liebowitz, H., pp. 48-220.

Mohr, D., Henn, S., 2007. Calibration of stress-triaxiality dependent crack formation criteria: A new hybrid experimental-numerical method. *Exp. Mech.* **47**, 805-820.

Mohr, D., Oswald, M., 2008. A new experimental technique for multiaxial testing of advanced high strength steels. *Exp. Mech.* **48**, 65-77.

Nahshon, K. and Hutchinson, J.W., 2008. Modification of the Gurson model for shear failure. *Eur. J. Mech. A/Solids* **27**, 1-17.

Rice, J.R. and Tracey, D.M., 1969. On the ductile enlargement of voids in triaxial stress fields. *J. Mech. Phys. Solids* **17**, 201-217.

Tardif, N. and Kyriakides, S., 2012. Determination of anisotropy and material hardening for aluminum sheet metal. *Int'l J. Solids Struct.* in press doi: 10.1016/j.ijsolstr.2012.01.011.

Vander Voort, G. F., and E. P. Manilova. Metallographic Etching of Aluminum and Its Alloys. *Metallography Papers*. N.p., n.d. Web. Spring 2012. <http://www.georgevandervoort.com/metallography_papers.html>.

Vita

Scott Sumner Haltom was born and raised in Mississippi. He graduated from St Andrew's Episcopal School in 2006 before attending the University of Mississippi. He graduated from the Sally McDonnell Barksdale Honors College at Ole Miss while also playing varsity baseball for the Rebels. In the fall of 2010, after graduating from Ole Miss, he enrolled in the Graduate School at the University of Texas at Austin to pursue a Master of Science degree in Engineering Mechanics. In the fall of 2012, he moved to Houston, Texas to accept a position with Stress Engineering Services Inc.

This thesis was typed by the author.